Radiative forcing of anthropogenic aerosols on cirrus clouds using a hybrid ice nucleation scheme

Jialei Zhu[1] and Joyce E. Penner[1]

1 Department of Climate and Space Sciences and Engineering, University of Michigan, Ann Arbor, Michigan 48109, USA

Correspondence to: Jialei Zhu (jialeiz@umich.edu)

Abstract

Anthropogenic aerosols impact cirrus clouds through ice nucleation, thereby changing the Earth's radiation budget. However, the magnitude and sign of anthropogenic forcing on cirrus clouds are still very uncertain depending on the treatments for ice nucleating particles (INPs) and the ice nucleation scheme. In this study, a new ice nucleation scheme (hereafter the HYBRID scheme) is developed to combine the best features of two previous ice nucleation schemes, so that the global model is able to calculate the ice number concentration in both the updrafts and downdrafts associated with gravity waves and has a robust sensitivity to the change of aerosol number. The ice number concentrations calculated using the HYBRID scheme are overestimated somewhat but are in reasonable agreement with an adiabatic parcel model and observations. The forcing and cloud changes associated with changes in aircraft soot, sulfur emission and all anthropogenic emissions between the preindustrial period (PI) and the present day (PD) are examined using a global model with the HYBRID scheme. Aircraft soot emissions decrease the global average ice number concentration (Ni) by $-1.0\pm2.4\times10^7$ m^{-2} due to the inhibition of homogeneous nucleation and lead to a radiative forcing of -0.14 ± 0.07 W m^{-2}, while

25   the increase in the sulfur emissions increases the global average Ni by $7.3\pm2.9\times10^7$

26   m^{-2} due to the increase in homogeneous nucleation and leads to a radiative forcing

27   of -0.02 ± 0.06 W m^{-2}. The possible effects of aerosol and cloud feedbacks to the

28   meteorological state in remote regions partly contribute to reduce the forcing and the

29   change in Ni due to anthropogenic emissions. The radiative forcing due to all

30   increased anthropogenic emissions from PI to PD is estimated to be -0.20 ± 0.05 W

31   m^{-2}. If newly formed secondary organic aerosols (SOA) acts an INP and inhibit

32   homogeneous nucleation, the Ni formed from heterogeneous nucleation is increased.

33   As a result, the inclusion of INPs from SOA increases the change in Ni to

34    $12.0\pm2.3\times10^7$ m^{-2} and increases (makes less negative) the anthropogenic forcing on

35   cirrus clouds to -0.04 ± 0.08 W m^{-2} from PI to PD.

1. Introduction

38   Atmospheric aerosol loading has increased significantly since the preindustrial

39   period (PI), mainly due to anthropogenic emissions associated with the burning of

40   fossil fuels and biomass. Most studies to date have focused on how the increase in

41   anthropogenic aerosols impacts climate via warm clouds thereby exerting a net

42   cooling effect (Wang and Penner, 2009;Zhu et al., 2019;Gordon et al., 2016;IPCC,

43   2013). Compared to warm clouds, there has been much less attention paid to

44   anthropogenic forcing as a result of changes to cirrus clouds, which is one of the

45   least understood processes in the climate system (Fan et al., 2016). Cirrus clouds

46   cover about 30% of the Earth's area (Wang et al., 1996) and play an important role

47   in the Earth's radiation budget and also influence global precipitation and the

48   hydrologic cycle (Waliser et al., 2009). Ice particles in cirrus clouds are nucleated

49   on aerosol particles, so that changes to the aerosol composition and loading may

50 alter cirrus clouds by altering cloud microphysics resulting in a cirrus cloud radiative

51 forcing.

52   There remain major uncertainties in calculating the radiative forcing of cirrus

53 clouds using global climate models (GCMs), both in terms of its magnitude (since

54 PI) and its sign (Storelvmo, 2017). The ice particles in the cirrus clouds can form

55 either by homogeneous freezing of solution droplets (Koop et al., 2000) or by

56 heterogeneous nucleation of INPs (Cantrell and Heymsfield, 2005). Supercooled

57 aqueous solutions such as sulfate haze particles can form ice through homogeneous

58 nucleation when the relative humidity with respect to ice (RHi) is high (of order

59 150%), which may be the dominant mechanism for the ice formation in the

60 atmosphere (Hendricks et al., 2011;Penner et al., 2018). However, heterogeneous ice

61 nucleation of INPs formed from dust, soot and other insoluble aerosols requires

62 much lower RHi, so that heterogeneous nucleation is able to occur in advance of

63 homogeneous nucleation in a rising air parcel (Hoose and Möhler, 2012). As a result,

64 heterogeneous and homogeneous ice formation compete for the available water

65 vapor. Heterogeneous nucleation can lead to a significant reduction of the number

66 of ice particles that form compared to homogeneous freezing because the number of

67 INPs is much smaller than the number of haze particles. However, if additional INPs

68 are added to a region where heterogeneous nucleation already dominates, an increase

69 in ice crystal number is expected. Therefore, the radiative effect of aerosols on cirrus

70 clouds could differ in both magnitude and sign depending on the competition

71 between these two ice nucleation processes, which is determined by both the number

72 of homogeneous and heterogeneous ice nucleating particles as well as the aerosol

73 composition and the updraft velocity or cooling rate.

74   Despite the relatively low level of understanding of ice nucleation, a few

75 physically based parameterizations that treat the competition between homogeneous

76   and heterogeneous nucleation have been developed in order to study the global effect

77   of ice nucleation in GCMs (Liu and Penner, 2005;Kärcher et al., 2006;Barahona and

78   Nenes, 2008). The Liu and Penner (2005) parameterization (hereafter LP) is derived

79   from fitting the simulation results of an adiabatically rising cloud parcel (Liu and

80   Penner, 2005). The LP parameterization is only able to treat cases for which the

81   updraft velocity is positive, so the evaporation of drops during downdrafts is

82   neglected in the LP parameterization. The parameterization developed by Barahona

83   and Nenes (2008) (hereafter BN) is derived from an analytical solution of the cloud

84   parcel equations (Barahona and Nenes, 2008). The LP and BN parameterizations

85   always show a similar trend when there is an increase in either the haze aerosol

86   number concentration or INPs, (Shi and Liu, 2018) and they result in very similar

87   ice number concentrations when the water vapor accommodation coefficient is set

88   to 0.1 (Zhou et al., 2016). The Kärcher et al. (2006) parameterization (hereafter KL)

89   explicitly calculates the evolution of ice supersaturation in a rising cloud parcel when

90   different aerosol types freeze (Kärcher et al., 2006). The KL parameterization was

91   used in previous studies of the effect of aerosol particles on cirrus clouds because it

92   includes an explicit representation of the relevant physics (Penner et al., 2009;Penner

93   et al., 2018) and Penner et al. (2018) added the capability to represent evaporation

94   of water in downdrafts. However, in the KL parameterization, aerosol particles in

95   different size bins will freeze chronologically from the largest size bin until the rate

96   at which RHi decreases by water vapor deposition equals the rate at which RHi

97   increases as a result of temperature decreases. Under this assumption, competition

98   among different aerosol size bins for water deposition is not allowed. As a result, the

99   homogeneous freezing of some particles in small size bins is underestimated in KL

100   parametrization (Liu and Shi, 2018). The KL parametrization results in a smaller

101   sensitivity   to   increases   in   sulfate   aerosol   number   than   the   LP   and   BN

102   parametrizations except at very low sulfate number concentrations, while the three

103   parameterizations have similar sensitivity to the number concentration of INPs (Shi
104   and Liu, 2018).

105   Global numerical simulation experiments of aerosol effects on cirrus cloud
106   formation have been carried out in limited studies with different ice nucleation
107   parameterizations and updraft treatments. Penner et al. (2009) used the KL and LP
108   parameterizations to estimate the radiative forcing of aerosols on cirrus clouds using
109   an off-line radiative transfer model. They found a negligible forcing from sulfate but
110   a significant cooling ranging from -0.38 to -0.56 W m^{-2} from surface-based and
111   aircraft emissions of soot with the assumption that 100% of soot particles are
112   efficient INPs (Penner et al., 2009). As a result, the radiative forcing of all
113   anthropogenic aerosols was estimated to be -0.53 to -0.67 W m^{-2} using the LP and
114   KL parameterizations. However, observations now indicate that only 0.01 to 0.1%
115   of the less-hygroscopic soot from fossil fuels and biomass fires act as good INPs at
116   supersaturations near 140% RHi and low temperatures (Koehler et al., 2009;Pratt et
117   al., 2011;Prenni et al., 2012). Gettelman et al. (2012) used the LP and BN
118   parameterization and calculated that the radiative forcing associated of aerosol
119   effects on cirrus clouds is 0.27±0.10 W m^{-2} as a consequence of increasing
120   anthropogenic sulfur emissions (with no effect from soot) (Gettelman et al., 2012).

121   In addition to assumptions of the extent to which soot might act as an INP, a
122   second source of uncertainty in the calculation of aerosol forcing in cirrus clouds is
123   the treatment of the sub-grid scale updraft velocity used in the nucleation scheme
124   (Zhou et al., 2016). Penner et al. (2009) used a normal probability distribution with
125   a standard deviation of 0.33 m s^{-1} (Penner et al., 2009) while Wang and Penner (2010)
126   used a single updraft velocity based on the standard deviation of mesoscale
127   temperature fluctuations associated with gravity waves (Wang and Penner, 2010).
128   Other models choose a sub-grid scale updraft velocity associated with the predicted

129   turbulent kinetic energy (Liu et al., 2012). Penner et al. (2018) first used a wave

130   spectrum instead of a constant updraft velocity based on KL parameterization with

131   the spectrum of observed gravity waves presented by Podglajen et al. (2016) together

132   with the seasonal and latitudinal variations determined by Gary (2006) and Gary

133   (2008), which accounts for the fluctuations of vertical velocities as well as the

134   vertical stratification of atmospheric stability. However, the radiative forcing of

135   sulfate as well as all anthropogenic aerosols were not explored due to the deficiencies

136   in the KL parameterization (Liu and Shi, 2018).

137   Secondary organic aerosols (SOA) have been shown to have a highly viscous

138   semisolid or even glassy states at low temperatures and low RHi in many

139   experiments (Koop et al., 2011;Pajunoja et al., 2014;Renbaum-Wolff et al.,

140   2013;Saukko et al., 2012). Observations also found SOA in the ice crystal residues

141   of cirrus clouds and acting as IN to form ice particles (Ignatius et al., 2016;Wagner

142   et al., 2017;DeMott et al., 2003;Cziczo et al., 2013;Wilson et al., 2012). A peak in

143   the number concentration of ultrafine particles were observed near 12km in the

144   Amazon and identified as primarily organic. Furthermore, a marker molecule

145   indicated that a substantial fraction of organics in aerosol-rich layers in the upper

146   troposphere were associated with the oxidation of isoprene (Andreae et al., 2018). A

147   modelling study that included organic nucleation predicted that there are plenty

148   number of accumulation mode SOA particles existing in the upper tropical

149   troposphere which may be important for the ice nucleation (Zhu and Penner, 2019).

150   SOA particles have a strong potential to act as INPs to form ice particles via

151   heterogeneous freezing under the conditions conducive to ice formation in the upper

152   troposphere (Knopf et al., 2018). The radiative forcing of anthropogenic aerosols in

153   warm clouds might be significantly reduced when SOA is included (Zhu et al.,

154 2019;Gordon et al., 2016), but the influence of SOA on cirrus clouds is not yet fully

155 studied (but see Penner et al., 2018).

156   In this study, we combined the best features of the LP and KL parameterizations

157 to develop a hybrid ice nucleation scheme that accounts for the changes in ice

158 number concentrations in both the updrafts and downdrafts associated with a

159 spectrum of gravity waves. Using a global climate model coupled with the new ice

160 nucleation scheme, the radiative forcing of aircraft soot and sulfate were examined.

161 Furthermore, the radiative forcing of anthropogenic aerosols on cirrus clouds since

162 the PI time period was estimated including the effect of changes in SOA. A global

163 average negative anthropogenic forcing of -0.203 ± 0.052 m^{-2} as a result of aerosol

164 effects in cirrus clouds is suggested. The forcing is reduced to -0.039 ± 0.075 W m^{-2}

165 when SOA is included.

166

2. Methodology

168 2.1 Model

169   We used the Community Earth System model (CESM) version 1.2.2 coupled to

170 the University of Michigan IMPACT aerosol model with resolution of 1.9°

171 (longitude)×2.5° (latitude) to simulate aerosols and their effects on cirrus clouds.

172 This version of the IMPACT model simulates the number and mass of pure sulfate

173 in three modes (i.e. nucleation (<5 nm), Aitken (5-50 nm) and accumulation (>50

174 nm)) and their interaction with fourteen other aerosol species/types. Sulfate is the

175 only aerosol participating in homogeneous ice nucleation in the model. Soot from

176 fossil fuel and biofuel burning (fSoot) is simulated in three modes with different

177 hygroscopicity according to the number of monolayers sulfate on its surface while

178   soot from biomass burning (bSoot) is simulated in one mode. 0.05% of fSoot with

179   <1 monolayers of sulfate and 0.1% of fSoot with 1-3 monolayers of sulfate as well

180   as 0.1% of bSoot are assumed to be effective INPs. Aircraft soot is simulated in two

181   modes. One mode has acted as an ice nuclei within contrails that subsequently

182   evaporated. The other mode has not been an ice nuclei within contrails. We assume

183   the soot that has already been included in contrail ice is pre-activated and could

184   subsequently form an ice particle at 145% relative humidity with respect to ice. Pre-

185   activated aircraft soot with less than 3 monolayers of sulfate, which has a high ice

186   nucleation activity (Mahrt et al., 2019), is assumed to be an INP similar to the

187   treatment in Zhou and Penner (2014). Dust and sea salt are each carried in four

188   separate bins with varying radii. Dust with fewer than 3 monolayers of sulfate

189   coating is used to form heterogeneous INP in the model. The aerosols simulated by

190   the IMPACT model only interact with the physical processes that form cirrus clouds

191   in the CESM model, but the changes in cirrus clouds have feedback to the radiation

192   budget, temperature, the formation of warm clouds as simulated in the CESM model.

193

2.2 Ice nucleation parameterization

195   The LP parameterization is only able to calculate the ice nucleation in a rising

196   parcel, but not able to predict the changes in the supersaturation or simulate the

197   evaporation of ice in downdrafts. As a result, the scheme used by Penner et al. (2018)

198   to treat gravity waves cannot be used with the LP parameterization as it was

199   originally formulated. The KL scheme calculates the changes in the sub-grid scale

200   variation of RHi in a cloud parcel to simulate the growth or decay of preexisting ice

201   particles. However, aerosols freeze in the order of size bins and this neglects the

202   competition among different aerosol size bins , which results in an underestimation

203 of the ice formed from aerosols in small size bins and a low sensitivity to the change

204 of aerosol number (Liu and Shi, 2018). In this study, we combined the LP and KL

205 parameterizations to develop a new ice nucleation scheme (hereafter HYBRID) to

206 make use of their strengths and avoid their defects. In the HYBRID scheme, the

207 RHi in the cloud parcel is calculated explicitly using the KL scheme so that ice

208 particles are able to grow or decay throughout the time variations in the updrafts

209 and downdrafts associated with gravity waves. When the supersaturation is high

210 enough to enable ice nucleation, the LP parameterization is used to calculate the

211 increase in the ice number from homogeneous and/or heterogeneous freezing, so that

212 the HYBRID scheme avoids the lack of sensitivity to changes in aerosol number in

213 the KL parameterization when calculating the number of new ice particles. The

214 updraft velocity determines both the changes in the RHi (as determined in KL) and

215 the number of ice crystals (as determined in LP). We generated a series of updraft

216 velocities at each grid point based on a fitted wave spectrum from the observed

217 equatorial gravity waves of Podglajen et al. (2016) but extended their measurements

218 to other latitudes and seasons by using the parameterization proposed by (Gary,

219 2008, 2006). This parameterization of wave spectrum associated with gravity wave

220 is described in Penner et al. (2018).

221

222 ## 2.3 Experiments

223 We performed a series of model experiments in which different emissions of

224 aerosols and aerosol precursors are used. Table 1 provides a summary of these

225 experiments. The base case (PD_Base) uses emissions for the present day (PD,

226 ≈2000) for anthropogenic sulfur, soot from fossil fuel adopted from Community

227 Emission Data System (CEDS) (Hoesly et al., 2018) and from van Marle et al. (2017)

228 for biomass burning. We included soot from aircraft for 2006 based on the Aviation

229   Environment Design Tool data set (Barrett et al., 2010). The dimethylsulfide (DMS)

230   emissions from the ocean is assumed constant in the PD and PI (Tilmes et al., 2016).

231   The emission of dust uses the scheme from Zender et al. (2003). The emission of

232   cSoot is removed from PD_Base to examine its impact on ice number concentration

233   and radiative forcing (PI_cSoot). We also set a case (PI_SO4) with the emission of

234   anthropogenic sulfur changed to PI (≈1750) to calculate the radiative forcing of

235   sulfur. The case (PI_ALL) to examine the radiative forcing of all anthropogenic

236   aerosols on cirrus cloud is conducted with all emissions changed to PI (≈1750).

237   Additionally, we set up two experiments to examine the effect of SOA on the

238   anthropogenic forcing on cirrus cloud. The case PD_SOA and PI_SOA adds newly

239   formed SOA particles as additional INPs to the cases of PD_Base and PI_ALL

240   separately. The cases including SOA in the PD and PI read in the explicit number

241   concentration of newly formed SOA in the accumulation mode nucleated from

242   highly oxygenated organic molecules (HOMs), which were simulated using the

243   version of the CESM/IMPACT model outlined in Zhu et al. (2019) and Zhu and

244   Penner (2019). The SOA that meets the requirements of the glass transition

245   temperature and RHi calculated using the equations in Wang et al. (2012) acts as an

246   effective heterogeneous INP. All cases were run with winds nudged towards

247   ECMWF reanalysis data using a nudging time of 6 hours for the years 2005-2011

248   (Zhang et al., 2014). The data for the last six years were used for analysis in this

249   study.

250

3. Results

3.1 Ice number concentrations

In order to examine the ability of the HYBRID ice nucleation scheme to simulate ice number concentration, the results from an ice nucleation adiabatic model using the HYBRID scheme are compared with those from an adiabatic parcel model under the same simulation conditions. The adiabatic parcel model was used to generate the LP parameterization, which was introduced in Liu and Penner (2005). The two models are run for 30 min for each simulation, which is the time step used in the global model. During the 30 min, the updraft velocity is updated every 2.2 min as recommended by Podglajen et al. (2016). The ice number concentrations after 30 min simulation from the two models are compared. We run the parcel model using a constant updraft velocity for each 2.2-min interval when the velocity is positive, which is the same as the HYBRID scheme used in the global model. For downdrafts, if the supersaturation is below 100%, the two models use the same method to simulate the evaporation of pre-existing ice particles which is also the same method used in the global model as suggested in Kärcher et al. (2006). The updraft and downdraft associated gravity waves are determined from a Laplace distribution as suggested from gravity waves observation by Podglajen et al. (2016). There are 10,000 simulations conducted using random gravity waves using each model. Both models use the same gravity waves in each simulation. We set up an initial condition with a temperature of 230K, the standard deviation for the updraft velocities was 0.5 m s^{-1} and the initial RHi was 130%. The sulfate number concentration was set to 200 cm^{-3} while the dust concentration was 10 L^{-1}. These particles then participate in either homogeneous nucleation or heterogeneous immersion nucleation. Figure 1 shows a histogram of the predicted ice number concentration (Ni) for 10,000 simulations of the adiabatic parcel model and the box model using the HYBRID

277   scheme. Two populations of Ni are shown in the Figure 1. The lower population

278   (with of the order of 10 L^{-1} or less) represents primarily heterogeneous nucleation

279   on dust particles, while the higher population (with of the order of 10^2 L^{-1} or more)

280   represents primarily homogeneous nucleation on sulfate aerosols. The results in the

281   simulations dominated by heterogeneous nucleation are mostly similar for the two

282   models, although the HYBRID scheme overestimates the Ni between 1~10 L^{-1} when

283   the results from the parcel model are less than 10^{-1} L^{-1} for some of these same

284   simulations. The average Ni from heterogeneous nucleation over 10,000 simulations

285   from the parcel model is 9.40±2.31 L^{-1}, while that from the HYBRID scheme is

286   9.52±2.08 L^{-1}. The box model using the HYBRID scheme predicts larger Ni from

287   homogeneous nucleation than the parcel model in the 88% of simulations with

288   homogeneous nucleation occurring. There are more simulations using the HYBRID

289   scheme that predict larger Ni from homogeneous nucleation than the parcel model

290   as indicated by larger number of counts of large Ni (10^4 L^{-1} or more) in Figure 1.

291   The HYBRID scheme uses the LP parameterization for every small time step of 2.2

292   min. Since the LP parameterization was built using the largest Ni in an ascending

293   parcel after 30 min, there is a tendency for the HYBRID scheme to overpredict Ni.

294   The average Ni from homogeneous nucleation over the 1,337 simulations when

295   homogeneous nucleation occurs in the two models is 9.05±7.72×10^3 L^{-1} from the

296   parcel model, while it is10.99±8.28×10^3 L^{-1} from the box model using the HYBRID

297   scheme. The HYBRID scheme overestimates the Ni from homogeneous nucleation

298   by 21.5%. Overall, the average total Ni over the 10,000 simulations is 1.53±4.83 L^{-1}

299   using the HYBRID scheme, which is 7.3% larger than the result from the parcel

300   model (1.42±4.23 L^{-1}). Although the HYBRID scheme predicts a somewhat larger

301   number of nucleated ice particles, the results are reasonable compared to the results

302   from the parcel model.

303   The predicted Ni in PD_Base case is compared with the observed Ni in Figure

304   2. The observational data plotted in Figure 2 have been expanded to include more

305   flights than the data originally reported by Krämer et al. (2009) (Martina Krämer,

306   personal communication, 2018). Data from the model have been selected to have ice

307   water mixing ratios > 10^{-8} kg kg^{-1} to match values seen in the in-situ observations

308   (Krämer et al., 2016). The global model using the HYBRID scheme is able to do a

309   reasonable job in predicting the Ni for all temperatures except for the somewhat high

310   concentrations seen between 195K and 215K. The global average Ni in the PD_Base

311   is 0.15×10^{10} m^{-2} with the largest Ni in the tropics of Eastern Hemisphere (Figure 3a).

312   Most ice particles nucleate in the upper troposphere (150~200 hPa) in the tropics,

313   while some ice nucleation occurs in the lower troposphere (around 300 hPa) in the

314   polar regions (Figure 3b). The ice particles formed from homogeneous nucleation

315   dominate the total Ni in most regions over the world (Figure 4a) and are responsible

316   for ~95% of global average Ni (Figure 3c). Heterogeneous nucleation dominates the

317   Ni in the northern middle-high latitudes where anthropogenic soot emission is high

318   (Figure 4a), although the Ni from heterogeneous nucleation is high in the tropics

319   (Figure 3e). Homogeneous nucleation mostly occurs in the upper troposphere

320   (around 200hPa in the tropics and around 300hPa in the extratropical regions), while

321   heterogeneous nucleation is an important contributor to Ni in the middle and lower

322   troposphere (Figure 4b). Although the Ni from homogeneous nucleation is high, the

323   occurrence frequency of homogeneous nucleation is up to ~20% in the tropics and

324   < 5% in most other regions (Figure 4c).

325   The competition between the heterogeneous INPs and homogeneous haze

326   particles determines the change in Ni between the PD and PI periods. We set up three

327   sensitivity cases to separately examine the effects of the emission of cSoot for

328   aircraft, anthropogenic sulfur and all anthropogenic emissions on the Ni. INPs

329   always nucleate prior to homogeneous nucleation in a rising air parcel, so they

330   consume the available water vapor and inhibit homogeneous freezing in the regions

331   dominated by homogeneous nucleation. The Ni formed from heterogeneous

332   nucleation increases significantly around 200hPa over the world due to the inclusion

333   of INPs from cSoot, especially near Southeast Asia (Figure 5e, 5f). Simultaneously,

334   homogeneous nucleation is inhibited significantly around 200hPa in Southeast Asia

335   and other tropical regions (Figure 5c, 5d). The emission of aircraft soot that form

336   contrails are shown in Figure 1a in the Zhou and Penner (2014). Due to the much

337   larger decrease in Ni from homogeneous nucleation than the increase in Ni from

338   heterogeneous nucleation, the global average Ni is decreased by 0.1×10^8 m^{-2} when

339   including the emission of aircraft soot (Figure 5a).

340   In contrast to the case of aircraft soot, the increase in the sulfur emissions from

341   PI to PD leads to a significant increase in Ni from homogeneous nucleation in most

342   regions, which causes an increase of 1.01×10^8 m^{-2} in the global average Ni (Figure

343   6c). Although the decrease in Ni from heterogeneous nucleation offsets some of the

344   increase in Ni from homogeneous nucleation, the global average Ni is increased by

345   0.73×10^8 m^{-2} due to the increase in sulfur emissions.

346   The change in Ni from PI to PD due to all anthropogenic emissions is a balance

347   among the effects of increasing INPs from surface and aircraft soot as well as haze

348   particles. The effect of all anthropogenic emissions on Ni is mostly dominated by

349   the increase in Ni from homogeneous nucleation caused by the increase in sulfur

350   emissions, but homogeneous nucleation is inhibited somewhat by increased INPs

351   from soot (compare Figure 7c and 6c). As a result, the global average increase in Ni

352   from homogeneous nucleation between PD_Base and PI_ALL is only 58% of that

353   between PD_Base and PI_SO4. The change in Ni from heterogeneous nucleation is

354   decreased in the mid-high latitudes of the Northern Hemisphere (NH) from PD_Base

355   to PI_ALL similar to the decrease from PD_Base to PI_SO4 (Figure 7e, 7f).

356   However, the increase in INPs from soot near Southeast Asia leads to a small

357   increase in Ni from heterogeneous nucleation there. In total, the increase in all

358   anthropogenic emissions causes an increase of Ni in South Asia and the North Indian

359   Ocean as well as in polar regions while an decrease of Ni is found in mid-latitude

360   regions and tropical west Pacific Ocean, resulting in 0.49×10^8 m^{-2} more Ni from PI

361   to PD for the global average.

362   It is conspicuous that sulfur and aircraft soot emissions have effects with different

363   signs of the change in Ni (Figure 5a, 6a). Generally, INPs from aircraft soot decrease

364   Ni due to the suppression of homogeneous nucleation in the regions dominated by

365   homogeneous nucleation, while the increase in sulfur emissions increases Ni in these

366   same regions due to the enhancement of homogeneous nucleation. However, the

367   change in Ni have opposite signs in the west Pacific Ocean off the coast of Southeast

368   Asia, where the homogeneous nucleation is most active (Figure 3c). We attribute

369   this to the possible effect of aerosol and cloud feedbacks to the meteorological state.

370   When including aircraft soot, the temperature is decreased (Figure 8b) and the RHi

371   is increased (Figure 8a) around 150hPa over the west Pacific Ocean, where Ni from

372   homogeneous nucleation increases most significantly (Figure 5c). The decrease in

373   temperature is beneficial to homogeneous nucleation. Meanwhile, the emission of

374   aircraft soot is very low in the west Pacific Ocean due to the lack of flight routes

375   there (refer to the Figure 1a in the Zhou and Penner (2014)), so that the effect of

376   aircraft soot on the suppression of homogeneous nucleation is weak in that region

377   (Figure 5e). As a result, the Ni from homogeneous nucleation is increased, which

378   determines the increase in the Ni near 150 hPa over the west Pacific Ocean due to

379   the emission of aircraft soot (Figure 5a). Similarly, when the sulfur emissions are

380   increased from PI to PD, the change in cirrus clouds influence the meteorological

10.5194/acp-2019-1055
Atmospheric Chemistry and Physics
2020-01-03
Author(s) 2020. CC BY 4.0 License.

381   state. A significant decrease in RHi at 150hPa is found in the west Pacific Ocean

382   (Figure 9a), so that the occurrence frequency of homogeneous nucleation decreases

383   when sulfur emissions increase (Figure 9d). Additionally, the temperature at 150hPa

384   increases over the world (Figure 9b), which also contributes partly to the decrease

385   in the occurrence frequency of homogeneous nucleation. Although global sulfur

386   emissions increase sharply from PI to PD, the anthropogenic emissions mainly occur

387   on the mainland with much smaller emissions over the ocean. The column number

388   concentration of sulfate having the potential to freeze homogeneously do not

389   increase significantly over most ocean regions (Figure 9c), so that the decrease in

390   the occurrence frequency of homogeneous nucleation leads to a decrease in Ni from

391   homogeneous nucleation over the west Pacific Ocean (Figure 6c). The increase in

392   the temperature in the upper troposphere over the world (Figure 9b) also partly

393   explains the decrease in Ni from heterogeneous nucleation when only sulfur

394   emissions increase (Figure 6e). The feedback to the meteorological state in remote

395   regions always have an opposite effect on the changes in Ni compared to the effect

396   in regions with large anthropogenic emissions. These meteorological feedbacks

397   partly reduce the changes in global average Ni due to anthropogenic emissions.

398

3.2 Radiative forcing

400   The decrease in Ni in the upper troposphere usually leads to an increase in the

401   size of ice particles, which promotes the gravitational removal and formation of

402   snow, causing a decrease in the ice water path (IWP) and vice versa. As a result, the

403   change in IWP is mainly determined by the change in Ni and have a similar

404   geographic pattern. The emission of aircraft soot leads to a decrease in IWP in

405   Southeast Asia and the Caribbean Sea region, caused by the inhibition of

406   homogeneous nucleation, while the IWP increases in the west Pacific Ocean when

407   including the aircraft soot emissions because of the increase in Ni from

408   homogeneous nucleation as discussed above (Figure 10a). As shown in the Figure

409   11a, the increase in the sulfur emissions leads to a significant increase in IWP in the

410   north Indian Ocean and a decrease in the West Pacific Ocean due to the changes in

411   Ni from homogeneous nucleation. The decrease in IWP in the mid-high latitudes of

412   the NH is attributed to the decrease in Ni from heterogeneous nucleation (Figure

413   11a). The geographic pattern of changes in IWP due to all anthropogenic emissions

414   increase from PI to PD is dominated by the changes in IWP caused by the changes

415   in sulfur emissions (compare Figure 11a and 12a). However, the increase in IWP in

416   tropical regions is smaller and the decrease in IWP in mid-high latitudes of the NH

417   is more negative in the PD_Base-PI_ALL case compared to the PD_Base-PI_SO4

418   case because of the inhibition of homogeneous nucleation caused by the increase in

419   the emission of surface and aircraft soot. As a result, although the geographical

420   pattern of the changes in IWP is similar for the PD_Base-PI_ALL and PD_Base-

421   PI_SO4 cases, the magnitude of changes in the global average IWP changes from

422   positive (0.07 g m^{-2} for PD_Base-PI_SO4, Figure 11a) to negative (-0.13 g m^{-2} for

423   PD_Base-PI_ALL, Figure 12a).

424   The changes in the Ni and IWP lead to a change in the cirrus cloud fraction and

425   also feedback to the lapse rate of temperature, which have an effect on the delivery

426   of water vapor and the strength of convection and these changes influence the

427   formation and lifetime of liquid water clouds. The liquid water path (LWP) change

428   due to these complex dynamical feedbacks are shown in Figure 10b, Figure 11b and

429   Figure 12b. The changes in the shortwave and longwave radiative fluxes are

430   determined by the changes in LWP and IWP, although they are dominated by the

431   change in IWP. The changes in the all-sky shortwave forcing (FSNT) and longwave

432 forcing (FLNT) at the top of the atmosphere (TOA) generally follow the changes in

433 IWP but have the opposite sign (Figure 10, Figure 11 and Figure 12). The changes

434 in LWP could either enhance or offset the effect of changes in IWP on the radiative

435 fluxes depending on whether the sign of the changes in IWP and LWP are

436 reinforcing or not. The emission of cSoot leads to a positive global average FSNT

437 and negative global average FLNT mostly due to the decrease in the global average

438 IWP (Figure 10). On the other hand, the increase in the sulfur emissions causes a

439 negative global average FSNT and positive global average FLNT largely because of

440 the increase in the global average IWP (Figure 11). The changes in the FSNT and

441 FLNT due to the increase in all anthropogenic emissions have a similar geographic

442 pattern to those caused by the increase in sulfur emissions but the global average

443 forcings have opposite signs (compare Figure 11c, 11d and Figure 12c, 12d). This is

444 due to the decrease in the global average IWP caused by the inhibition of

445 homogeneous nucleation as a result of the increased emissions of soot.

446   The total net forcing (FNT) is determined by the balance of FSNT and FLNT.

447 The radiative forcing in cirrus clouds is mostly dominated by FLNT because of the

448 larger longwave radiative effects of cirrus cloud than their shortwave radiative

449 effects. However, it is still possible that the radiative forcing due to changes in Ni in

450 cirrus clouds in some regions is dominated by FSNT due to the combined effects on

451 shortwave forcing from the changes in cirrus clouds together with warm clouds

452 caused by feedbacks. The emission of cSoot has a negative global average FNT of -

453 0.141 ± 0.069 W m^{-2} in cirrus clouds with a significant contribution from the negative

454 FNT over the north Atlantic Ocean (Figure 10e). The FNT due to cSoot is most

455 negative around the 30°N where the emission of aircraft soot is high, while there is

456 a small positive forcing around 10°N dominated by FSNT (Figure 10f). Although

457 the increase in sulfur emissions from PI to PD leads to an increase in the global

458   average Ni and IWP, the global average FNT due to sulfur emissions is a small

459   negative, -0.025±0.064 W m^{-2}. The FNT due to sulfur emissions is large and positive

460   (up to 7.1 W m^{-2}) around the 30°N and a small positive number around the 20°S due

461   to the significant increase in sulfur emission over the mainland there (Figure 11e).

462   The FNT is negative over most mid to high latitudes of the NH, which is attributed

463   to the decrease in FLNT associated with the feedback to the decrease in Ni from

464   heterogeneous nucleation there. However, the negative FNT in the north Indian

465   Ocean and positive FNT in the west Pacific Ocean are dominated by the change in

466   FSNT (Figure 11c, 11e). The LWP increases in the north Indian Ocean and decrease

467   in the west Pacific Ocean as a result of dynamic feedbacks from the changes in the

468   cirrus clouds, leads to the significant FSNT in these two regions together with the

469   changes in IWP and cirrus clouds. The negative FNT in the north Indian Ocean and

470   mid to high latitudes of the NH offset the positive FNT around the 30°N and 20°S

471   (Figure 11e). When including the increased emissions of surface and aircraft soot,

472   the FNT is less positive in South Asia and more negative in the mid to high latitudes

473   of the NH and the north Indian Ocean (Figure 12e). In the mid to high latitudes of

474   the Southern Hemisphere (SH), FSNT and FLNT always cancel each other so that

475   FNT is negligible. As a result, the global average FNT due to the all increased

476   anthropogenic emissions from PI to PD is -0.203±0.052 W m^{-2}, which is mainly

477   dominated by the changes in FLNT (Figure 12e, 12f).

478

3.3 The influence of SOA on anthropogenic forcing

480   SOA particles have a strong potential to act as INPs and therefore influence on

481   the formation of cirrus clouds. We examined the radiative forcing of all

482   anthropogenic aerosols on cirrus clouds when including the INPs from SOA

483   particles. Figure 13 shows the column number concentration of INPs and zonal

484   average of INPs from SOA in the PD and PI atmosphere. The number concentration

485   of INPs from SOA is much higher in the PD than that in the PI due to the much

486   higher concentration of SOA in the accumulation mode in the PD (Zhu et al., 2019).

487   The INPs from SOA are highest in the middle latitude of the NH in the PD, while

488   the INPs from SOA are higher in the SH than that in the NH in the PI atmosphere

489   (Figure 13a, 13b). The INPs from SOA in the PD are spread from 600hPa to 150hPa

490   with a peak around 300hPa, so there is a possible influence on the formation of cirrus

491   clouds (Figure 13b). The INPs from SOA in the PI are distributed a little higher than

492   those in the PD (Figure 13d). The global average Ni from heterogeneous nucleation

493   increases by 1.86×10^8 m^{-2} from PI to PD when including the INPs from SOA (Figure

494   14e), instead of the decrease in the global average Ni from heterogeneous nucleation

495   in the case without SOA (Figure 7e). The INPs from SOA increase the Ni from

496   heterogeneous nucleation in both the PD and PI cases when compared to the

497   PD_Base and PI_ALL cases (Figure 15e, Figure 16e). However, the increase in the

498   Ni from heterogeneous nucleation in the PD is much larger than that in the PI

499   because of the high number concentration of INPs from SOA in the PD. As a result,

500   the large increase in the INPs from SOA from the PI to the PD enhances the

501   heterogeneous nucleation resulting in an increase in the Ni from heterogeneous

502   nucleation especially in the tropics around 150hPa and in Antarctic from 400hPa to

503   200hPa (Figure 14f). The increase in the heterogeneous nucleation when including

504   SOA inhibits the homogeneous nucleation widely in the PD and PI (Figure 15c,

505   Figure 16c). In the PD, the increase in the Ni from heterogeneous nucleation even

506   outweighs the decrease in the Ni from homogeneous nucleation leading to an

507   increase of 0.4×10^8 m^{-2} in the global average Ni due to SOA compared to the

508   PD_Base case (Figure 15). In comparison, the INPs from SOA in the PI case make

509   a larger contribution to the decrease in Ni from homogeneous nucleation than the

510 increase in Ni from heterogeneous nucleation resulting in a decrease of -0.31×10^8

511 m^{-2} compared to the PI_ALL case (Figure 16). The inclusion of INPs from SOA

512 decreases the Ni in the tropics but increases the Ni in the mid to high latitudes in

513 both the NH and SH (Figure 15b, 16b). The global average Ni in the PD increases

514 while the global average Ni in the PI is decreased. Both changes are caused by

515 additional INPs from SOA (Figure 15a, 16a) resulting in a larger increase in the

516 global average Ni from PI to PD compared to the case without SOA (compare Figure

517 7a and Figure 14a). When including INPs from SOA, the Ni increases more

518 significantly in south Asia, the north Indian Ocean and Antarctica due to the increase

519 in heterogeneous nucleation, while the Ni decreases more significantly in the west

520 Pacific Ocean due to the stronger inhibition of homogeneous nucleation (compare

521 Figure 14a and Figure 7a).

522   The increased Ni leads to an increase in the IWP in south Asia, the north Indian

523 Ocean and Antarctica due to the reduction of gravitational removal, while the IWP

524 decrease in the middle latitude of the NH is caused by the decrease in Ni (Figure

525 17a). Compared with the case without SOA (PD_Base-PI_ALL), inclusion of SOA

526 increases the difference in the IWP between the PD and PI in Antarctica significantly

527 because of the increase in the Ni from heterogeneous nucleation of INPs from SOA

528 there (Figure 18b). In addition, the larger decrease in the Ni from homogeneous

529 nucleation in the tropics when including SOA compared to the case without SOA

530 causes the larger decrease in the IWP (Figure 18b). The difference in the LWP due

531 to dynamic feedbacks between the cases with and without SOA is not very

532 significant (Figure 18c). The larger increases in Ni and IWP in the tropics of the NH

533 lead to the larger changes in both FSNT and FLNT when including SOA compared

534 to the case without SOA, while the increase in Ni and IWP in Antarctica and the

535 Arctic only change the FLNT significantly but not the FSNT because of the very

536 low shortwave flux in the polar areas (Figure 18d, 18e). The larger decrease in the

537 FSNT offsets the increase in the FLNT in the tropics when including SOA resulting

538 in a similar value for FNT in the tropics for the cases with and without SOA (Figure

539 18f). However, the more positive changes in the FLNT from PI to PD in Antarctica

540 and the Arctic when including SOA explain the more positive FNT there compared

541 to the case without SOA (Figure 18f). In addition, the FNT around 30ºN, where FNT

542 is most positive in the case without SOA, becomes more positive when including

543 SOA due to the larger increase in the Ni. As a result, the larger positive FNT in the

544 Antarctica, Arctic as well as in south Asia and north Africa around 30ºN cause the

545 increase in the global average FNT due to all anthropogenic aerosol to -0.039±0.075

546 W m^{-2} when including SOA from the -0.203±0.052 W m^{-2} in the case without SOA.

547 The FNT when including SOA is up to 6.6 W m^{-2} in the Arabian Peninsula while it

548 is as low as -4.8 W m^{-2} in the north Indian Ocean (Figure 17e).

549

4. Conclusion and discussion

551   This work develops a new ice nucleation parameterization, HYBRID, which is

552 a combination of the LP and KL parameterizations. The global model using this new

553 scheme is able to simulate the growth and decay of ice particles in the updrafts and

554 downdrafts associated with gravity waves as in the modified KL scheme (Penner et

555 al., 2018), and is able to treat the changes in aerosol number concentration with

556 fidelity in the sign of the change as in the LP scheme. The HYBRID scheme

557 overcomes some of the deficiencies in previous ice nucleation schemes. We

558 evaluated the HYBRID ice nucleation scheme by comparing the scheme with the

559 Liu and Penner (2005) adiabatic parcel model and by comparing its global

560 predictions using observed Ni. The parcel model simulations show that the HYBRID

561 predicts 7.3% larger Ni than the LP adiabatic parcel model with 21.5% larger Ni

562 from homogeneous nucleation over 10,000 simulations. The global model using
563 HYBRID scheme overestimates somewhat the Ni between 195K and 215K
564 compared to observations. The results of Ni from the HYBRID scheme are in
565 reasonable agreement with observations and thus were used in the global model to
566 estimate the radiative forcing of aerosol on cirrus clouds. The predicted Ni depends
567 on the competition between homogeneous and heterogeneous nucleation. These two
568 ice nucleation processes dominate the Ni in different regions and altitudes. The
569 global average Ni is dominated by homogeneous nucleation in the PD atmosphere.

570 We performed a series of model experiments using the HYBRID ice nucleation
571 scheme to explore the forcing and cloud changes associated with changes in aircraft
572 soot, sulfur emissions and all anthropogenic emissions from the PI to PD. Results
573 are summarized in the Table 2. The INPs from aircraft soot usually decrease the Ni
574 by the inhibition of homogeneous nucleation in spite of some areas with small
575 increases in Ni. In contrast, the increase in sulfur emissions from PI to PD enhances
576 homogeneous nucleation in most regions and leads to a small decrease in the Ni
577 formed as a result of heterogeneous nucleation. We found the possible effect of
578 aerosol and cloud feedbacks to the meteorological state such as temperature and RHi
579 could have an opposite effect on the changes in Ni due to either aircraft soot or sulfur
580 emissions in the remote regions like the west Pacific Ocean. These meteorological
581 feedbacks partly reduce the changes in the global average Ni due to anthropogenic
582 emissions. The changes in Ni from PI to PD caused by all anthropogenic emissions
583 are dominated by the changes due to the sulfur emissions but the changes in surface
584 and aircraft soot emission have some effects on the inhibition of homogeneous
585 nucleation.

586 The changes in Ni due to anthropogenic aerosols lead to changes in IWP as
587 well as LWP due to dynamical feedbacks. The changes in FSNT and FLNT are
588 always determined by the changes in the IWP, but the changes in LWP could either

589 enhance or offset the effects of IWP on the radiative fluxes. Emissions of aircraft

590 soot lead to a positive change in the global average FSNT while the global average

591 FLNT is negative. The changes in sulfur emissions from PI to PD leads to opposite

592 changes in the global average FSNT and FLNT compared to aircraft soot because of

593 the different signs of changes in Ni. The total net forcing in cirrus clouds is usually

594 dominated by FLNT but it is dominated by FSNT when the changes in warm clouds

595 cause a feedback that reinforces the effect of cirrus clouds on shortwave flux. As a

596 result, the emission of aircraft soot has a negative global average FNT of -0.14±0.07

597 W m^{-2} in cirrus clouds, while the changes in the sulfur emission from PI to PD lead

598 to a small negative global average FNT of -0.02±0.06 W m^{-2}. The global average

599 FNT due to all anthropogenic emissions from PI to PD, which is estimated to be -

600 0.20±0.05 W m^{-2}, is dominated by the FNT caused by increased sulfur emissions but

601 is more negative than the forcing by sulfur emissions alone due to the emission of

602 soot.

603   The influence of SOA on the anthropogenic forcing on cirrus clouds is examined.

604 The additional INPs from SOA increase the Ni from heterogeneous nucleation and

605 decrease the Ni from homogeneous nucleation, but the sign of the changes in the

606 total Ni depends on the balance of these two effects. The high number concentration

607 of INPs from SOA in the PD atmosphere causes an increase in the Ni while the low

608 number concentration in the PI atmosphere causes a decrease. As a result, the

609 changes in Ni due to the changes in anthropogenic emission from PI to PD become

610 larger when including INPs from SOA than the case without SOA. The inclusion of

611 SOA mainly increases the changes in FNT in the polar regions and the regions

612 around 30ºN, resulting in a less negative FNT of -0.04±0.07 W m^{-2} due to the

613 changes in all anthropogenic emissions.

614   The radiative forcing of anthropogenic emissions on cirrus clouds estimated in

615 this study is less negative than the result indicated in Penner et al. (2009) (-0.38 to -

616 0.56 W m^{-2}) and has a different sign compared with the result shown in Gettelman

617 et al. (2012) (0.27±0.10 W m^{-2}). This is mostly caused by the different treatments

618 for updraft velocity, haze particles, and INPs as well as the application of a different

619 ice nucleation scheme. Current models show that homogeneous nucleation

620 dominates the formation of new ice particles in most regions over the world with the

621 largest contribution to cirrus cloud formation in the tropical upper troposphere (Zhou

622 et al., 2016;Shi and Liu, 2018;Shi et al., 2015). However, some observation indicated

623 the importance and high occurrence frequency of heterogeneous nucleation in the

624 tropical tropopause region (Jensen et al., 2013). Although the inclusion of INPs from

625 newly formed SOA in this study inhibits homogeneous nucleation in the tropics,

626 homogeneous nucleation is still responsible for 75% of total Ni in the PD atmosphere.

627 Laboratory measurements have supported other species acting as INP and enhancing

628 heterogeneous nucleation such as solid ammonium sulfate (Abbatt et al., 2006),

629 which has not been considered in current global climate models. The additional INPs

630 can be expected to increase the anthropogenic forcing in cirrus clouds to be less

631 negative and possibly even positive. The HYBRID ice nucleation scheme

632 overestimates somewhat the ice number concentration produced from homogeneous

633 nucleation compared to a full parcel model. An explicit representation of the ice

634 nucleation process used in the global climate model may be helpful to predict the ice

635 number and therefore radiation budget more correctly in the future. The ability of

636 SOA to act as an INP probably varies depends on the property of different SOA

637 compounds as well as their particle size and mixing state (Baustian et al.,

638 2013;Berkemeier et al., 2014;Charnawskas et al., 2017;Shiraiwa et al., 2017). A

639 global climate model coupled online with the formation mechanism of SOA together

640 with an increased understanding of the ability of SOA to act as an INP would help

641 in estimating the contribution of SOA to the ice particle formation more accurately.

642

Author contribution

JZ developed the model, performed the simulations, analyzed all data and wrote a majority of the paper. JP guided the model development and data analysis and helped with writing paper.

Acknowledgments

We are grateful for funding from the NASA ACMAP program under grant number NNX15AE34G as well as an NSF-GEO grant number 1540954. Computer time was provided by the NCAR CISL.

References

Abbatt, J., Benz, S., Cziczo, D., Kanji, Z., Lohmann, U., and Möhler, O.: Solid ammonium sulfate aerosols as ice nuclei: A pathway for cirrus cloud formation, Science, 313, 1770-1773, 2006.

Andreae, M. O., Afchine, A., Albrecht, R., Holanda, B. A., Artaxo, P., Barbosa, H. M. J., Borrmann, S., Cecchini, M. A., Costa, A., Dollner, M., Fütterer, D., Järvinen, E., Jurkat, T., Klimach, T., Konemann, T., Knote, C., Krämer, M., Krisna, T., Machado, L. A. T., Mertes, S., Minikin, A., Pöhlker, C., Pöhlker, M. L., Pöschl, U., Rosenfeld, D., Sauer, D., Schlager, H., Schnaiter, M., Schneider, J., Schulz, C., Spanu, A., Sperling, V. B., Voigt, C., Walser, A., Wang, J., Weinzierl, B., Wendisch, M., and Ziereis, H.: Aerosol characteristics and particle production in the upper troposphere over the Amazon Basin, Atmospheric Chemistry and Physics, 18, 921-961, 10.5194/acp-18-921-2018, 2018.

Barahona, D., and Nenes, A.: Parameterization of cirrus cloud formation in large-scale models: Homogeneous nucleation, Journal of Geophysical Research: Atmospheres, 113, 2008.

Barrett, S., Prather, M., Penner, J., Selkirk, H., Balasubramanian, S., Dopelheuer, A., Fleming, G., Gupta, M., Halthore, R., and Hileman, J.: Guidance on the use of AEDT gridded aircraft emissions in atmospheric models, A technical note submitted to the US Federal Aviation Administration, Massachusetts Institute of Technology (MIT), 2010.

Baustian, K. J., Wise, M. E., Jensen, E. J., Schill, G. P., Freedman, M. A., and Tolbert, M. A.: State transformations and ice nucleation in amorphous (semi-)solid organic aerosol, Atmospheric Chemistry and Physics, 13, 5615-5628, 10.5194/acp-13-5615-2013, 2013.

Berkemeier, T., Shiraiwa, M., Pöschl, U., and Koop, T.: Competition between water uptake and ice nucleation by glassy organic aerosol particles, Atmospheric Chemistry and Physics, 14, 12513-12531, 10.5194/acp-14-12513-2014, 2014.

Cantrell, W., and Heymsfield, A.: Production of ice in tropospheric clouds: A review, Bulletin of the American Meteorological Society, 86, 795-808, 2005.

Charnawskas, J. C., Alpert, P. A., Lambe, A. T., Berkemeier, T., O'Brien, R. E., Massoli, P., Onasch, T. B., Shiraiwa, M., Moffet, R. C., Gilles, M. K., Davidovits, P., Worsnop, D. R., and Knopf, D. A.: Condensed-phase biogenic-anthropogenic

interactions with implications for cold cloud formation, Faraday Discuss, 200, 165-194, 10.1039/c7fd00010c, 2017.

Cziczo, D. J., Froyd, K. D., Hoose, C., Jensen, E. J., Diao, M., Zondlo, M. A., Smith, J. B., Twohy, C. H., and Murphy, D. M.: Clarifying the dominant sources and mechanisms of cirrus cloud formation, Science, 340, 1320-1324, 2013.

DeMott, P., Cziczo, D., Prenni, A., Murphy, D., Kreidenweis, S., Thomson, D., Borys, R., and Rogers, D.: Measurements of the concentration and composition of nuclei for cirrus formation, Proceedings of the National Academy of Sciences, 100, 14655-14660, 2003.

Fan, J., Wang, Y., Rosenfeld, D., and Liu, X.: Review of aerosol–cloud interactions: Mechanisms, significance, and challenges, Journal of the Atmospheric Sciences, 73, 4221-4252, 2016.

Gary, B. L.: Mesoscale temperature fluctuations in the stratosphere, Atmospheric Chemistry and Physics, 6, 4577-4589, 2006.

Gary, B. L.: Mesoscale temperature fluctuations in the Southern Hemisphere stratosphere, Atmospheric Chemistry and Physics, 8, 4677-4681, 2008.

Gettelman, A., Liu, X., Barahona, D., Lohmann, U., and Chen, C.: Climate impacts of ice nucleation, Journal of Geophysical Research: Atmospheres, 117, 10.1029/2012jd017950, 2012.

Gordon, H., Sengupta, K., Rap, A., Duplissy, J., Frege, C., Williamson, C., Heinritzi, M., Simon, M., Yan, C., Almeida, J., Trostl, J., Nieminen, T., Ortega, I. K., Wagner, R., Dunne, E. M., Adamov, A., Amorim, A., Bernhammer, A. K., Bianchi, F., Breitenlechner, M., Brilke, S., Chen, X., Craven, J. S., Dias, A., Ehrhart, S., Fischer, L., Flagan, R. C., Franchin, A., Fuchs, C., Guida, R., Hakala, J., Hoyle, C. R., Jokinen, T., Junninen, H., Kangasluoma, J., Kim, J., Kirkby, J., Krapf, M., Kurten, A., Laaksonen, A., Lehtipalo, K., Makhmutov, V., Mathot, S., Molteni, U., Monks, S. A., Onnela, A., Perakyla, O., Piel, F., Petaja, T., Praplan, A. P., Pringle, K. J., Richards, N. A., Rissanen, M. P., Rondo, L., Sarnela, N., Schobesberger, S., Scott, C. E., Seinfeld, J. H., Sharma, S., Sipila, M., Steiner, G., Stozhkov, Y., Stratmann, F., Tome, A., Virtanen, A., Vogel, A. L., Wagner, A. C., Wagner, P. E., Weingartner, E., Wimmer, D., Winkler, P. M., Ye, P., Zhang, X., Hansel, A., Dommen, J., Donahue, N. M., Worsnop, D. R., Baltensperger, U., Kulmala, M., Curtius, J., and Carslaw, K. S.: Reduced anthropogenic aerosol radiative forcing caused by biogenic new particle formation, Proc Natl Acad Sci U S A, 113, 12053-12058, 10.1073/pnas.1602360113, 2016.

723 Hendricks, J., Kärcher, B., and Lohmann, U.: Effects of ice nuclei on cirrus clouds
724 in a global climate model, Journal of Geophysical Research, 116,
725 10.1029/2010jd015302, 2011.

726 Hoesly, R. M., Smith, S. J., Feng, L., Klimont, Z., Janssens-Maenhout, G., Pitkanen,
727 T., Seibert, J. J., Vu, L., Andres, R. J., and Bolt, R. M.: Historical (1750–2014)
728 anthropogenic emissions of reactive gases and aerosols from the Community
729 Emissions Data System (CEDS), Geoscientific Model Development (Online), 11,
730 2018.

731 Hoose, C., and Möhler, O.: Heterogeneous ice nucleation on atmospheric aerosols:
732 a review of results from laboratory experiments, Atmospheric Chemistry and
733 Physics, 12, 9817-9854, 10.5194/acp-12-9817-2012, 2012.

734 Ignatius, K., Kristensen, T. B., Jarvinen, E., Nichman, L., Fuchs, C., Gordon, H.,
735 Herenz, P., Hoyle, C. R., Duplissy, J., Garimella, S., Dias, A., Frege, C., Hoppel, N.,
736 Troestl, J., Wagner, R., Yan, C., Amorim, A., Baltensperger, U., Curtius, J.,
737 Donahue, N. M., Gallagher, M. W., Kirkby, J., Kulmala, M., Mohler, O., Saathoff,
738 H., Schnaiter, M., Tome, A., Virtanen, A., Worsnop, D., and Stratmann, F.:
739 Heterogeneous ice nucleation of viscous secondary organic aerosol produced from
740 ozonolysis of alpha-pinene, Atmospheric Chemistry and Physics, 16, 6495-6509,
741 10.5194/acp-16-6495-2016, 2016.

742 IPCC: Climate Change 2013: The Physical Science Basis. Contribution of Working
743 Group I to the Fifth Assessment Report of the Intergovernmental Panel on Climate
744 Change, Cambridge University Press, Cambridge, United Kingdom and New York,
745 NY, USA, 1535 pp., 2013.

746 Jensen, E. J., Diskin, G., Lawson, R. P., Lance, S., Bui, T. P., Hlavka, D., McGill,
747 M., Pfister, L., Toon, O. B., and Gao, R.: Ice nucleation and dehydration in the
748 Tropical Tropopause Layer, Proc Natl Acad Sci U S A, 110, 2041-2046,
749 10.1073/pnas.1217104110, 2013.

750 Kärcher, B., Hendricks, J., and Lohmann, U.: Physically based parameterization of
751 cirrus cloud formation for use in global atmospheric models, Journal of Geophysical
752 Research, 111, 10.1029/2005jd006219, 2006.

753 Knopf, D. A., Alpert, P. A., and Wang, B.: The Role of Organic Aerosol in
754 Atmospheric Ice Nucleation: A Review, ACS Earth and Space Chemistry, 2, 168-
755 202, 10.1021/acsearthspacechem.7b00120, 2018.

756 Koehler, K. A., DeMott, P. J., Kreidenweis, S. M., Popovicheva, O. B., Petters, M.
757 D., Carrico, C. M., Kireeva, E. D., Khokhlova, T. D., and Shonija, N. K.: Cloud
758 condensation nuclei and ice nucleation activity of hydrophobic and hydrophilic soot
759 particles, Physical Chemistry Chemical Physics, 11, 7906-7920, 2009.

760 Koop, T., Luo, B. P., Tsias, A., and Peter, T.: Water activity as the determinant for
761 homogeneous ice nucleation in aqueous solutions, Nature, 406, 611-614,
762 10.1038/35020537, 2000.

763 Koop, T., Bookhold, J., Shiraiwa, M., and Poschl, U.: Glass transition and phase
764 state of organic compounds: dependency on molecular properties and implications
765 for secondary organic aerosols in the atmosphere, Phys Chem Chem Phys, 13,
766 19238-19255, 10.1039/c1cp22617g, 2011.

767 Krämer, M., Schiller, C., Afchine, A., Bauer, R., Gensch, I., Mangold, A., Schlicht,
768 S., Spelten, N., Sitnikov, N., and Borrmann, S.: Ice supersaturations and cirrus cloud
769 crystal numbers, Atmospheric Chemistry and Physics, 9, 3505-3522, 2009.

770 Krämer, M., Rolf, C., Luebke, A., Afchine, A., Spelten, N., Costa, A., Meyer, J.,
771 Zoeger, M., Smith, J., and Herman, R. L.: A microphysics guide to cirrus clouds-
772 Part 1: Cirrus types, Atmospheric Chemistry and Physics, 16, 3463-3483, 2016.

773 Liu, X., and Penner, J. E.: Ice nucleation parameterization for global models,
774 Meteorologische Zeitschrift, 14, 499-514, 2005.

775 Liu, X., Easter, R. C., Ghan, S. J., Zaveri, R., Rasch, P., Shi, X., Lamarque, J. F.,
776 Gettelman, A., Morrison, H., Vitt, F., Conley, A., Park, S., Neale, R., Hannay, C.,
777 Ekman, A. M. L., Hess, P., Mahowald, N., Collins, W., Iacono, M. J., Bretherton, C.
778 S., Flanner, M. G., and Mitchell, D.: Toward a minimal representation of aerosols in
779 climate models: description and evaluation in the Community Atmosphere Model
780 CAM5, Geoscientific Model Development, 5, 709-739, 10.5194/gmd-5-709-2012,
781 2012.

782 Liu, X., and Shi, X.: Sensitivity of homogeneous ice nucleation to aerosol
783 perturbations and its implications for aerosol indirect effects through cirrus clouds,
784 Geophysical Research Letters, 45, 1684-1691, 2018.

785 Mahrt, F., Kilchhofer, K., Marcolli, C., Grönquist, P., David, R. O., Rösch, M.,
786 Lohmann, U., and Kanji, Z. A.: The Impact of Cloud Processing on the Ice
787 Nucleation Abilities of Soot Particles at Cirrus Temperatures, Journal of
788 Geophysical Research: Atmospheres, 2019.

Pajunoja, A., Malila, J., Hao, L. Q., Joutsensaari, J., Lehtinen, K. E. J., and Virtanen, A.: Estimating the Viscosity Range of SOA Particles Based on Their Coalescence Time, Aerosol Sci. Technol., 48, I-IV, 10.1080/02786826.2013.870325, 2014.

Penner, J. E., Chen, Y., Wang, M., and Liu, X.: Possible influence of anthropogenic aerosols on cirrus clouds and anthropogenic forcing, Atmospheric Chemistry and Physics, 9, 879-896, 2009.

Penner, J. E., Zhou, C., Garnier, A., and Mitchell, D. L.: Anthropogenic Aerosol Indirect Effects in Cirrus Clouds, Journal of Geophysical Research: Atmospheres, 123, 11,652-611,677, 10.1029/2018jd029204, 2018.

Podglajen, A., Hertzog, A., Plougonven, R., and Legras, B.: Lagrangian temperature and vertical velocity fluctuations due to gravity waves in the lower stratosphere, Geophysical Research Letters, 43, 3543-3553, 2016.

Pratt, K., Murphy, S., Subramanian, R., DeMott, P., Kok, G., Campos, T., Rogers, D., Prenni, A., Heymsfield, A., and Seinfeld, J.: Flight-based chemical characterization of biomass burning aerosols within two prescribed burn smoke plumes, Atmospheric Chemistry and Physics, 11, 12549-12565, 2011.

Prenni, A. J., DeMott, P. J., Sullivan, A. P., Sullivan, R. C., Kreidenweis, S. M., and Rogers, D. C.: Biomass burning as a potential source for atmospheric ice nuclei: Western wildfires and prescribed burns, Geophysical Research Letters, 39, 2012.

Renbaum-Wolff, L., Grayson, J. W., Bateman, A. P., Kuwata, M., Sellier, M., Murray, B. J., Shilling, J. E., Martin, S. T., and Bertram, A. K.: Viscosity of alpha-pinene secondary organic material and implications for particle growth and reactivity, Proc. Natl. Acad. Sci. U. S. A., 110, 8014-8019, 10.1073/pnas.1219548110, 2013.

Saukko, E., Lambe, A. T., Massoli, P., Koop, T., Wright, J. P., Croasdale, D. R., Pedernera, D. A., Onasch, T. B., Laaksonen, A., Davidovits, P., Worsnop, D. R., and Virtanen, A.: Humidity-dependent phase state of SOA particles from biogenic and anthropogenic precursors, Atmospheric Chemistry and Physics, 12, 7517-7529, 10.5194/acp-12-7517-2012, 2012.

Shi, X., Liu, X., and Zhang, K.: Effects of pre-existing ice crystals on cirrus clouds and comparison between different ice nucleation parameterizations with the Community Atmosphere Model (CAM5), Atmospheric Chemistry and Physics, 15, 1503-1520, 10.5194/acp-15-1503-2015, 2015.

Shi, X., and Liu, X.: Sensitivity Study of Anthropogenic Aerosol Indirect Forcing through Cirrus Clouds with CAM5 Using Three Ice Nucleation Parameterizations, Journal of Meteorological Research, 32, 693-706, 10.1007/s13351-018-8011-z, 2018.

Shiraiwa, M., Li, Y., Tsimpidi, A. P., Karydis, V. A., Berkemeier, T., Pandis, S. N., Lelieveld, J., Koop, T., and Pöschl, U.: Global distribution of particle phase state in atmospheric secondary organic aerosols, Nature Communications, 8, 15002, 10.1038/ncomms15002, 2017.

Storelvmo, T.: Aerosol Effects on Climate via Mixed-Phase and Ice Clouds, Annual Review of Earth and Planetary Sciences, 45, 199-222, 10.1146/annurev-earth-060115-012240, 2017.

Tilmes, S., Lamarque, J.-F., Emmons, L. K., Kinnison, D. E., Marsh, D., Garcia, R. R., Smith, A. K., Neely, R. R., Conley, A., Vitt, F., Val Martin, M., Tanimoto, H., Simpson, I., Blake, D. R., and Blake, N.: Representation of the Community Earth System Model (CESM1) CAM4-chem within the Chemistry-Climate Model Initiative (CCMI), Geoscientific Model Development, 9, 1853-1890, 10.5194/gmd-9-1853-2016, 2016.

van Marle, M. J. E., Kloster, S., Magi, B. I., Marlon, J. R., Daniau, A.-L., Field, R. D., Arneth, A., Forrest, M., Hantson, S., Kehrwald, N. M., Knorr, W., Lasslop, G., Li, F., Mangeon, S., Yue, C., Kaiser, J. W., and van der Werf, G. R.: Historic global biomass burning emissions for CMIP6 (BB4CMIP) based on merging satellite observations with proxies and fire models (1750–2015), Geoscientific Model Development, 10, 3329-3357, 10.5194/gmd-10-3329-2017, 2017.

Wagner, R., Höhler, K., Huang, W., Kiselev, A., Möhler, O., Mohr, C., Pajunoja, A., Saathoff, H., Schiebel, T., Shen, X., and Virtanen, A.: Heterogeneous ice nucleation of α-pinene SOA particles before and after ice cloud processing, Journal of Geophysical Research: Atmospheres, 122, 4924-4943, 10.1002/2016jd026401, 2017.

Waliser, D. E., Li, J. L. F., Woods, C. P., Austin, R. T., Bacmeister, J., Chern, J., Del Genio, A., Jiang, J. H., Kuang, Z., and Meng, H.: Cloud ice: A climate model challenge with signs and expectations of progress, Journal of Geophysical Research: Atmospheres, 114, 2009.

Wang, B., Lambe, A. T., Massoli, P., Onasch, T. B., Davidovits, P., Worsnop, D. R., and Knopf, D. A.: The deposition ice nucleation and immersion freezing potential

of amorphous secondary organic aerosol: Pathways for ice and mixed‐phase cloud formation, Journal of Geophysical Research: Atmospheres, 117, 2012.

Wang, M., and Penner, J. E.: Aerosol indirect forcing in a global model with particle nucleation, Atmospheric Chemistry and Physics, 9, 239-260, 2009.

Wang, M., and Penner, J. E.: Cirrus clouds in a global climate model with a statistical cirrus cloud scheme, Atmospheric Chemistry and Physics, 10, 5449-5474, 10.5194/acp-10-5449-2010, 2010.

Wang, P. H., Minnis, P., McCormick, M. P., Kent, G. S., and Skeens, K. M.: A 6-year climatology of cloud occurrence frequency from Stratospheric Aerosol and Gas Experiment II observations (1985 – 1990), Journal of Geophysical Research: Atmospheres, 101, 29407-29429, 1996.

Wilson, T. W., Murray, B. J., Wagner, R., Möhler, O., Saathoff, H., Schnaiter, M., Skrotzki, J., Price, H. C., Malkin, T. L., Dobbie, S., and Al-Jumur, S. M. R. K.: Glassy aerosols with a range of compositions nucleate ice heterogeneously at cirrus temperatures, Atmospheric Chemistry and Physics, 12, 8611-8632, 10.5194/acp-12-8611-2012, 2012.

Zender, C. S., Bian, H., and Newman, D.: Mineral Dust Entrainment and Deposition (DEAD) model: Description and 1990s dust climatology, Journal of Geophysical Research: Atmospheres, 108, 2003.

Zhang, K., Wan, H., Liu, X., Ghan, S. J., Kooperman, G. J., Ma, P.-L., Rasch, P. J., Neubauer, D., and Lohmann, U.: On the use of nudging for aerosol–climate model intercomparison studies, Atmospheric Chemistry and Physics, 14, 8631-8645, 2014.

Zhou, C., and Penner, J. E.: Aircraft soot indirect effect on large-scale cirrus clouds: Is the indirect forcing by aircraft soot positive or negative?, Journal of Geophysical Research-Atmospheres, 119, 11303-11320, 10.1002/2014jd021914, 2014.

Zhou, C., Penner, J. E., Lin, G., Liu, X., and Wang, M.: What controls the low ice number concentration in the upper troposphere?, Atmospheric Chemistry and Physics, 16, 12411-12424, 10.5194/acp-16-12411-2016, 2016.

Zhu, J., and Penner, J. E.: Global Modeling of Secondary Organic Aerosol With Organic Nucleation, Journal of Geophysical Research: Atmospheres, 124, 8260-8286, 2019.

887   Zhu, J., Penner, J. E., Yu, F., Sillman, S., Andreae, M. O., and Coe, H.: Decrease in
888   radiative forcing by organic aerosol nucleation, climate, and land use change, Nature
889   Communications, 10, 423, 10.1038/s41467-019-08407-7, 2019.

890

891   Table 1. Description of cases

Case name	Description
PD_Base	Emissions for the present day (≈2000) for anthropogenic sulfur, surface and aircraft soot
PI_cSoot	As in PD_Base without INPs from pre-activated aircraft soot in contrails
PI_SO4	As in PD_Base, but with the anthropogenic sulfur emission for the preindustrial period (≈1750)
PI_ALL	As in PD_Base, but with the anthropogenic sulfur emission and surface soot emission for the pre-industrial period (≈1750) and without aircraft soot
PD_SOA	As in PD_Base, but adding INPs from newly formed SOA particles in present day
PI_SOA	As in PI_ALL, but adding INPs from newly formed SOA particles in preindustrial period

892   Note: SOA=secondary organic aerosol; INP=ice nucleating particle.

893

894   Table 2. Forcing and cloud changes associated with changes in aircraft soot, sulfur

895   and all anthropogenic aerosols.

Parameter	PD_Base-PI_cSoot	PD_Base-PI_SO4	PD_Base-PI_ALL	PD_SOA-PI_SOA
Ni (10^7 m^{-2})	-1.000±2.400	7.260±2.875	4.930±1.801	11.963±2.289
IWP (g m^{-2})	-0.129±0.056	0.067±0.058	-0.125±0.035	-0.124±0.047
LWP (g m^{-2})	-0.188±0.038	0.164±0.070	-0.048±0.077	0.025±0.058
FSNT (W m^{-2})	0.349±0.125	-0.356±0.097	0.099±0.063	-0.137±0.105
FLNT (W m^{-2})	-0.489±0.088	0.331±0.049	-0.302±0.063	0.099±0.042
FNT (W m^{-2})	-0.141±0.069	-0.025±0.064	-0.203±0.052	-0.039±0.075

896

897

898

899

900
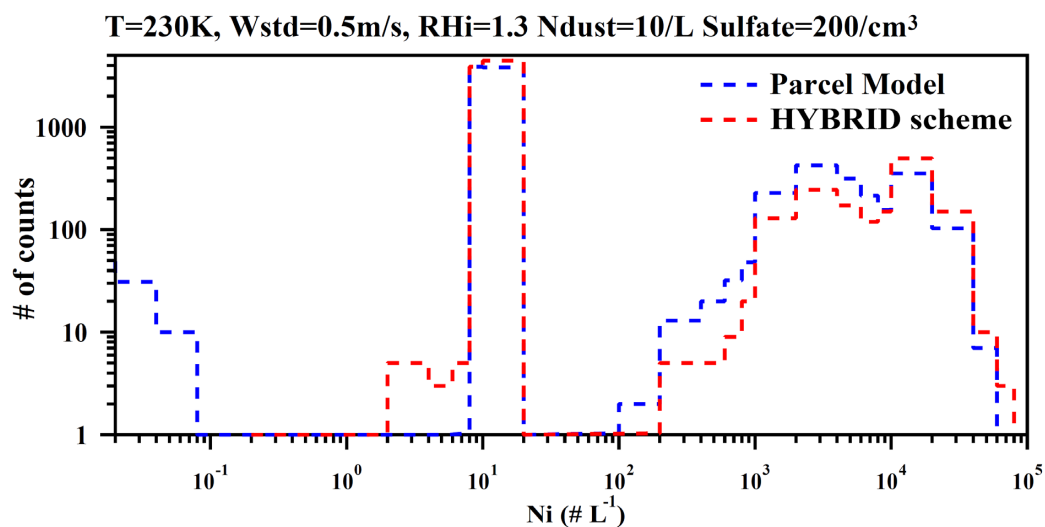
Figure 1. Histogram of predicted ice number concentration for 10,000 simulations 900 using an adiabatic parcel model (blue dashed line) and a box model using the HYBRID scheme (red dashed line). Wstd is the standard deviation of the assumed pdf of updraft velocities, while Ndust and Sulfate are the assumed dust and sulfate number concentrations.

906

907
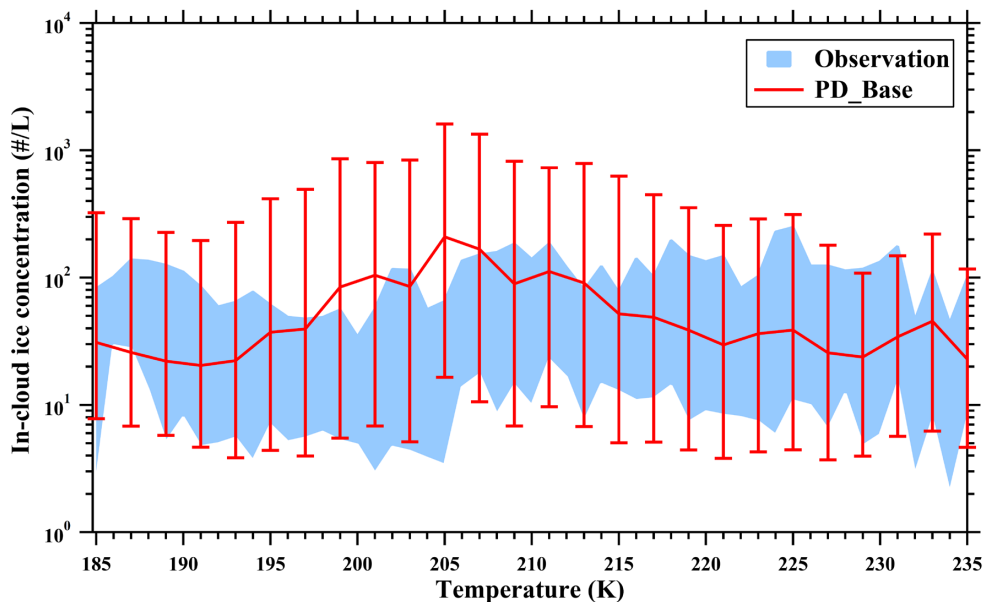
Figure 2. In-cloud ice crystal number concentration versus temperature from

PD_Base case with error bars of 25th and 75th percentiles. The background shaded

region shows the 25th-75th percentiles from an extended set of observations

originally compiled by Krämer et al. (2009).

912

913

914
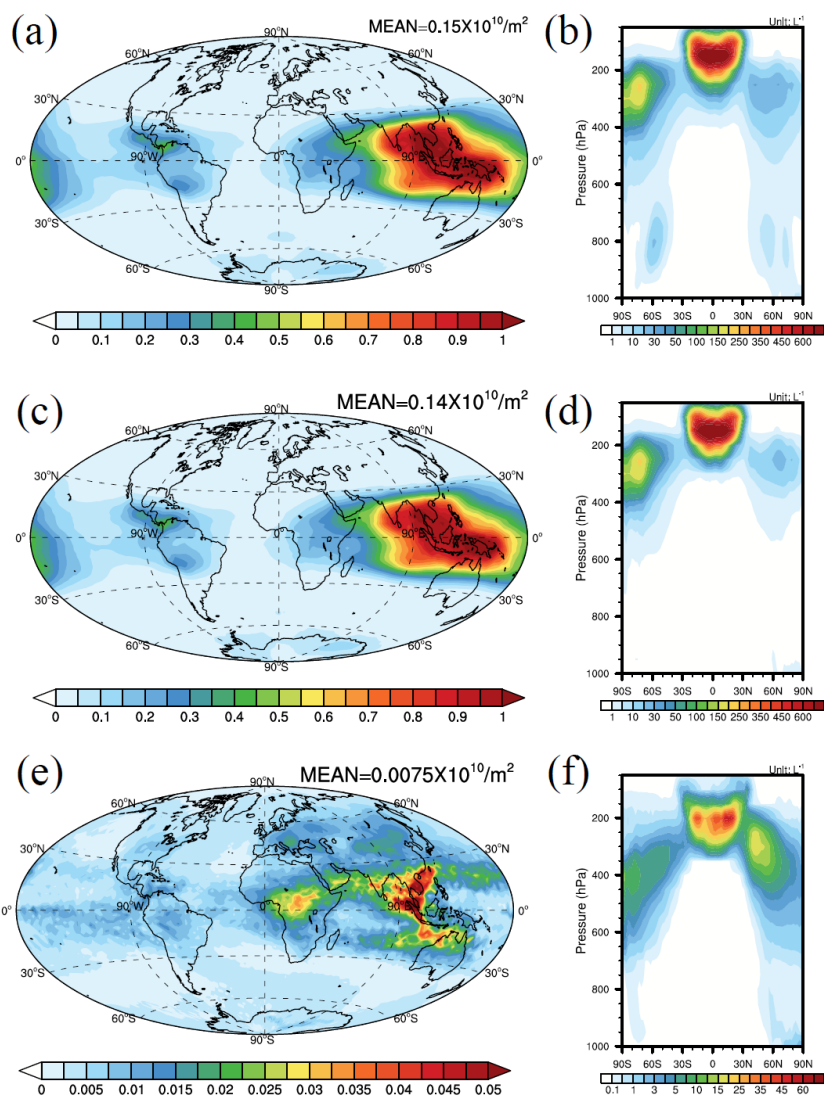
Figure 3. The vertically integrated total Ni in PD_Base case (a), Ni from
homogeneous nucleation (c) and Ni from heterogeneous nucleation (e). The zonal
average plots of Ni in PD_Base case (b), Ni from homogeneous nucleation (d) and
Ni from heterogeneous nucleation (f). Note: the vertical axis in (b), (d) and (f) are
in hybrid pressure levels
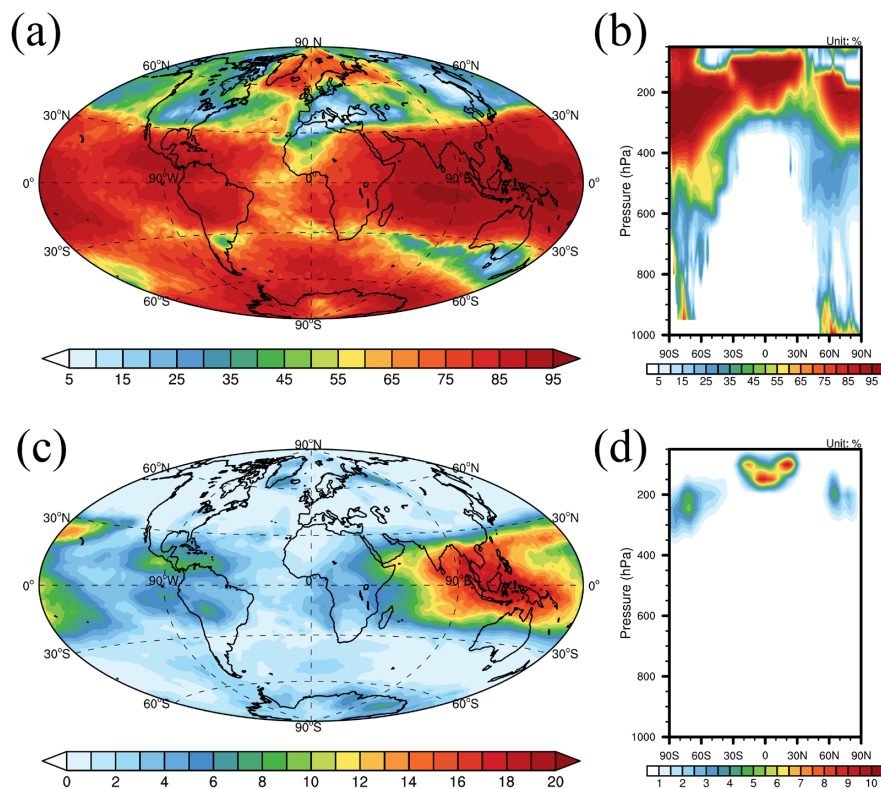
921

922 Figure 4. Vertically integrated percentage of new ice formed from homogeneous

923 nucleation (a) and the cloud-weighed occurrence frequency of homogeneous

924 nucleation (c) in the PD_Base case. The zonal average plots of percentage of new

925 ice formed from homogeneous nucleation (b) and cloud-weighed occurrence

926 frequency of homogeneous nucleation (d) in the PD_Base case.

927

928

929
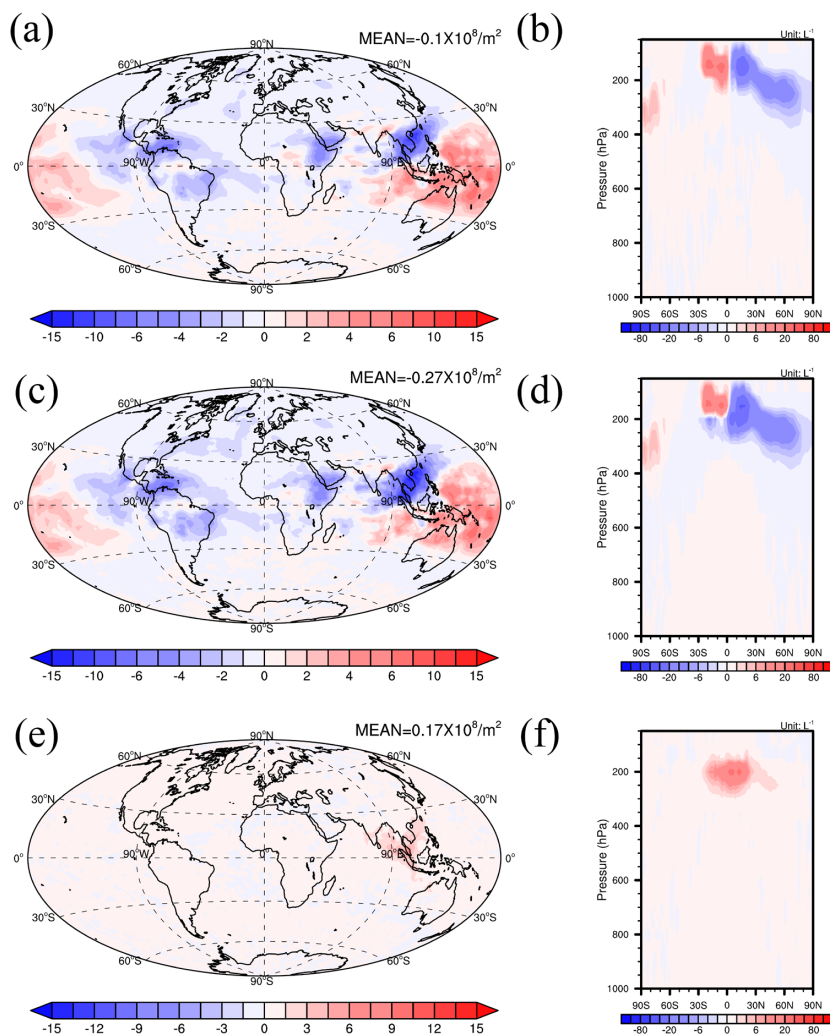
Figure 5. The annual average change in column number concentration (a, c, e) and zonal average number concentration (b, d, f) of total ice (a, b), ice from homogeneous nucleation (c, d) and ice from heterogeneous nucleation (e, f) for the difference between the PD_Base and PI_cSoot cases.

934

935

936
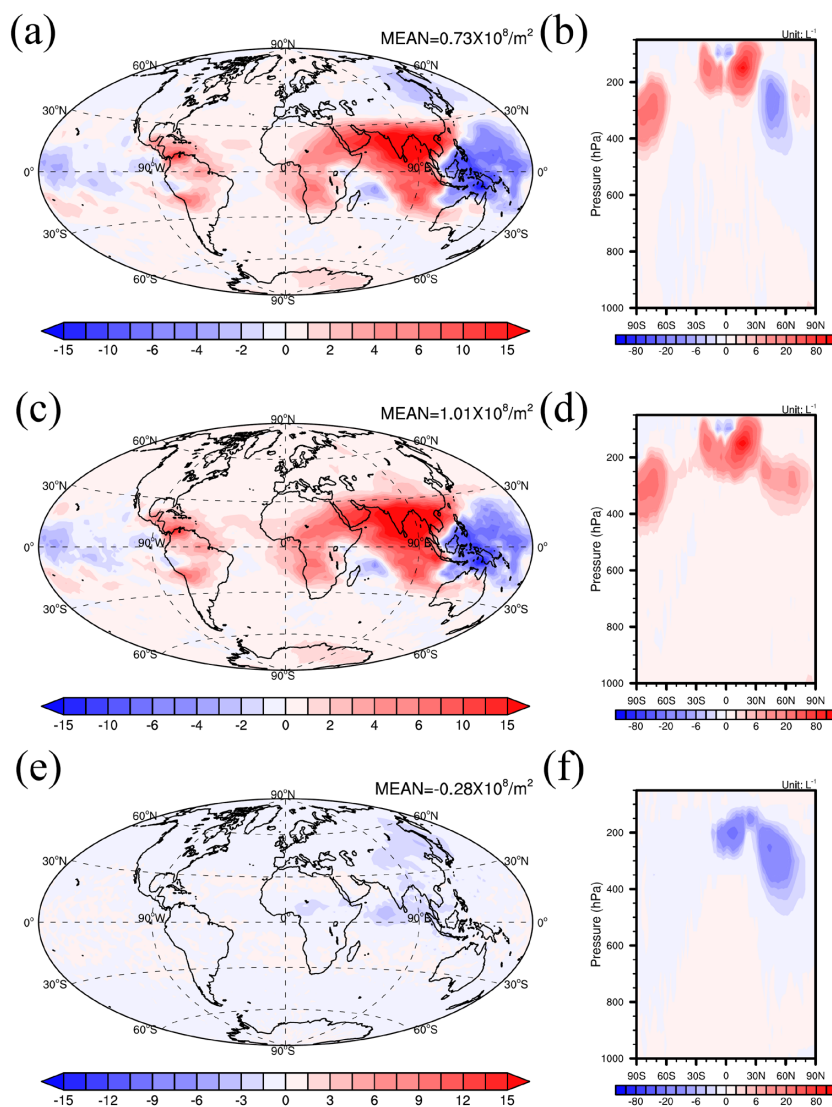
Figure 6. As in Figure 5 but for the difference between the PD_Base and PI_SO4

cases.

939

940

941
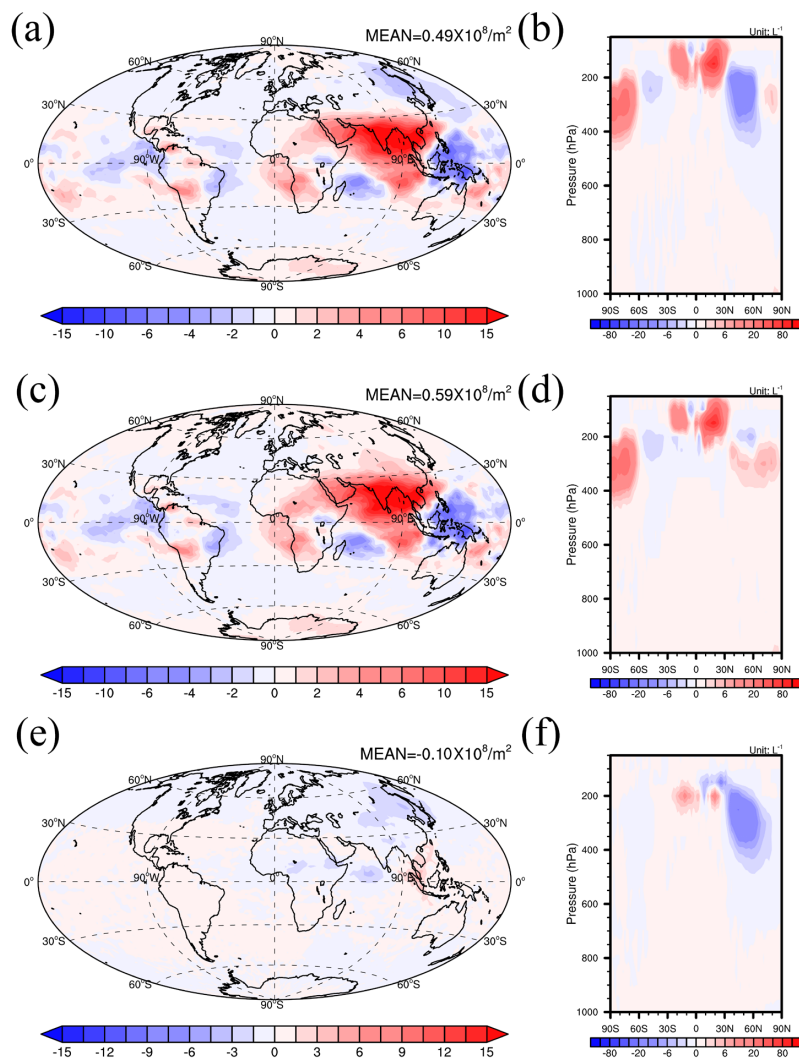
Figure 7. As in Figure 5 but for the difference between the PD_Base and PI_ALL

cases.

944

945
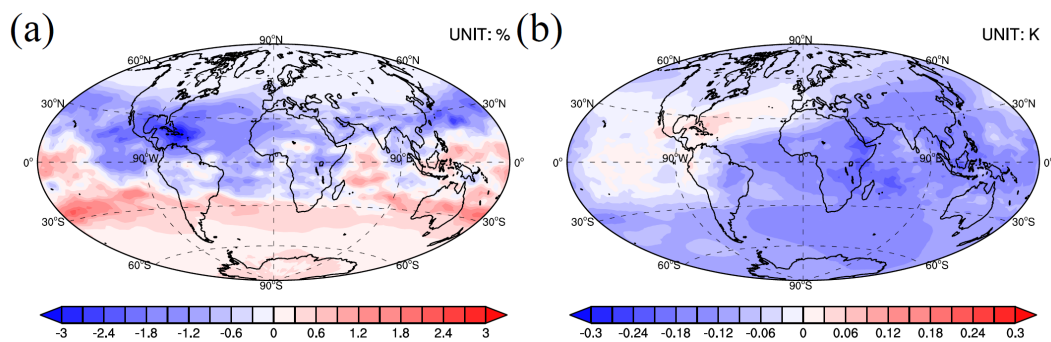
Figure 8. The annual average change in the RHi (a) and temperature (b) at 150 hPa for the difference between the PD_Base and PI_cSoot cases.

952
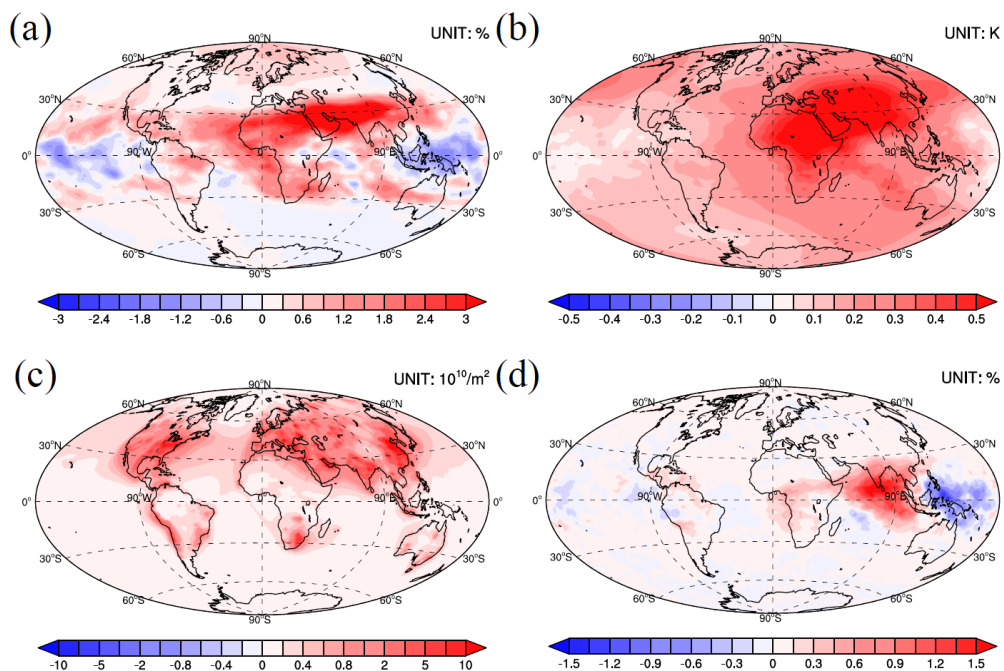
Figure 9. The annual average change in the RHi (a), temperature (b) and
occurrence frequency of homogeneous nucleation (d) at 150 hPa as well as
vertically integrated number concentration of sulfate in the Aitken and
accumulation mode (c) for the difference between the PD_Base and PI_SO4 cases.

957

958

959
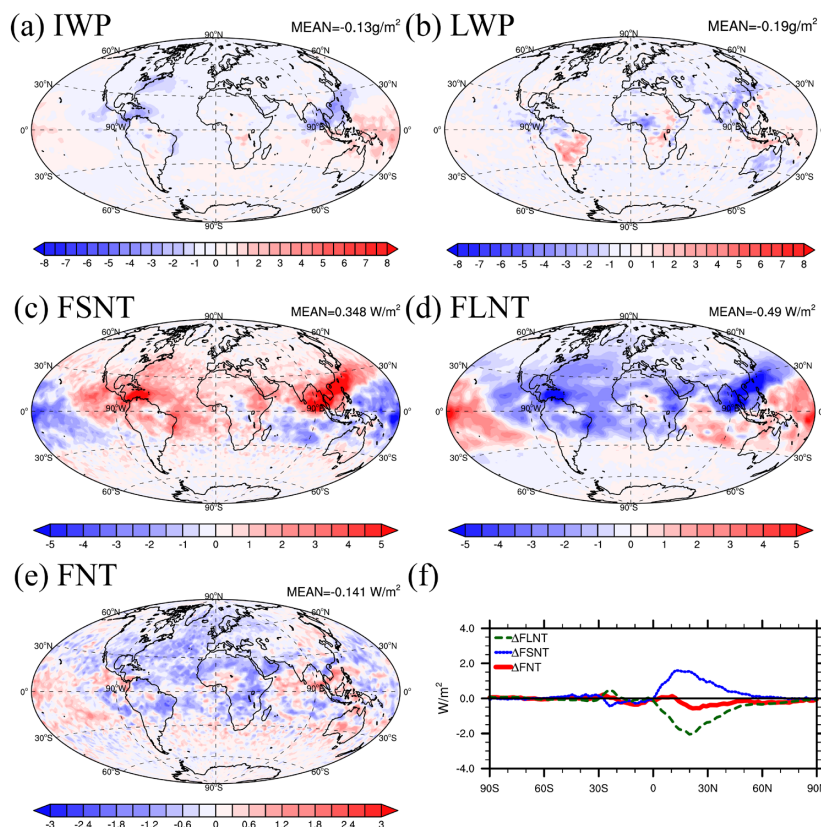
Figure 10. Annual mean plots of the change in vertically integrated averaged ice water path (a), liquid water path (b), net incoming shortwave radiation (c), long wave radiation (d) and net radiation (e) as well as shortwave effects (f, ΔFSNT, blue dotted line), longwave effects (f, ΔFLNT, green dashed line) and net effects (f, ΔFNT, red solid line) for the difference between the PD_Base and PI_cSoot cases.

969
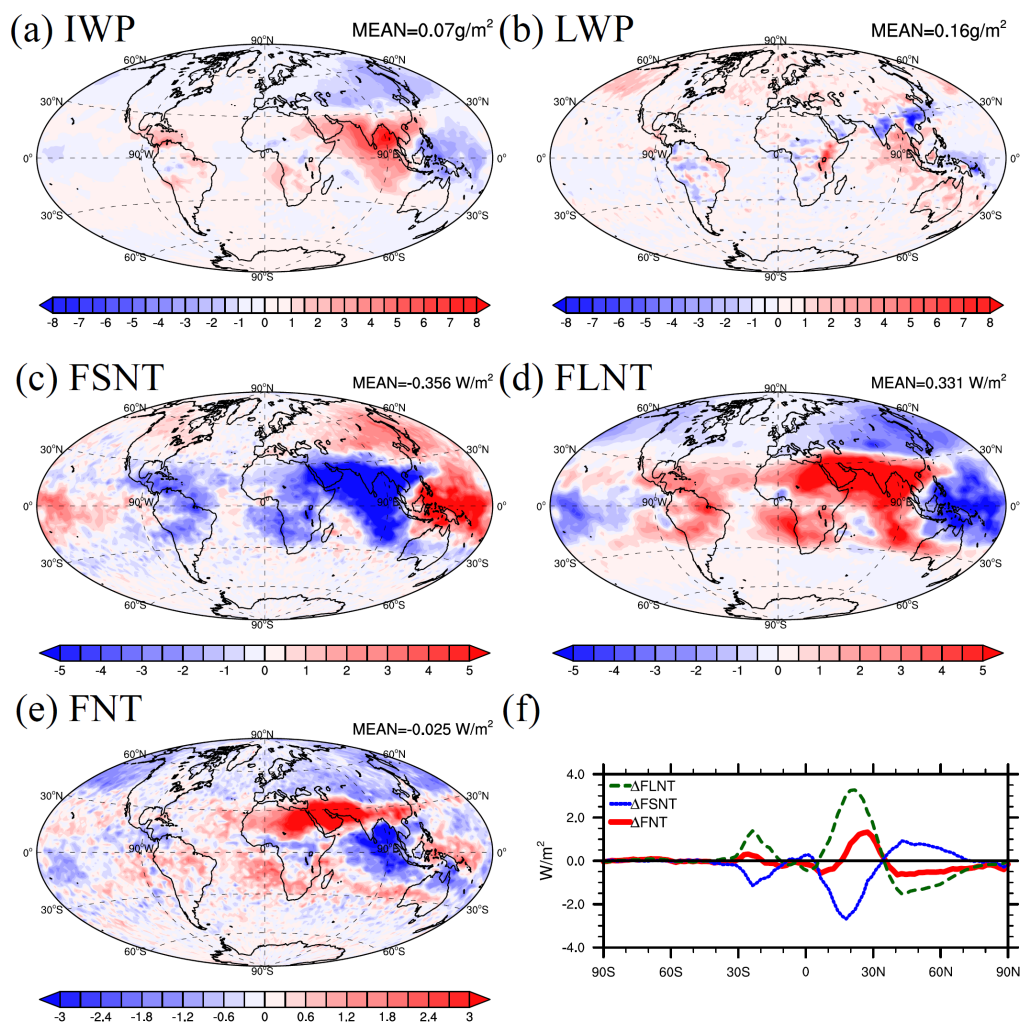
Figure 11. As in Figure 10 but for the difference between the PD_Base and
PI_SO4 cases.

970

971

972

973
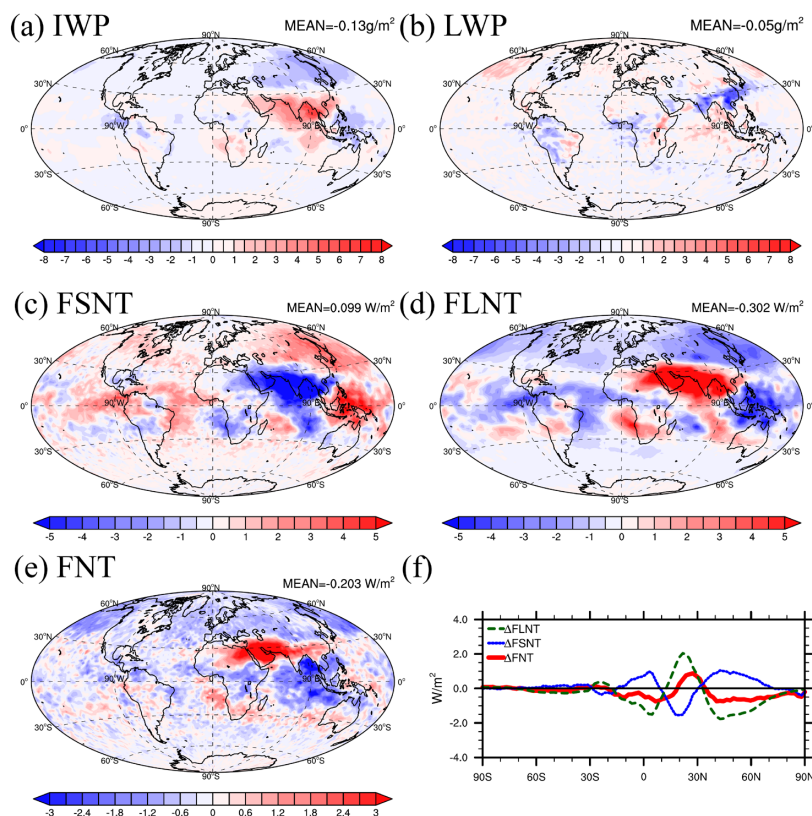
974

975 Figure 12. As in Figure 10 but for the difference between the PD_Base and

976 PI_ALL cases.

977

978

979

980
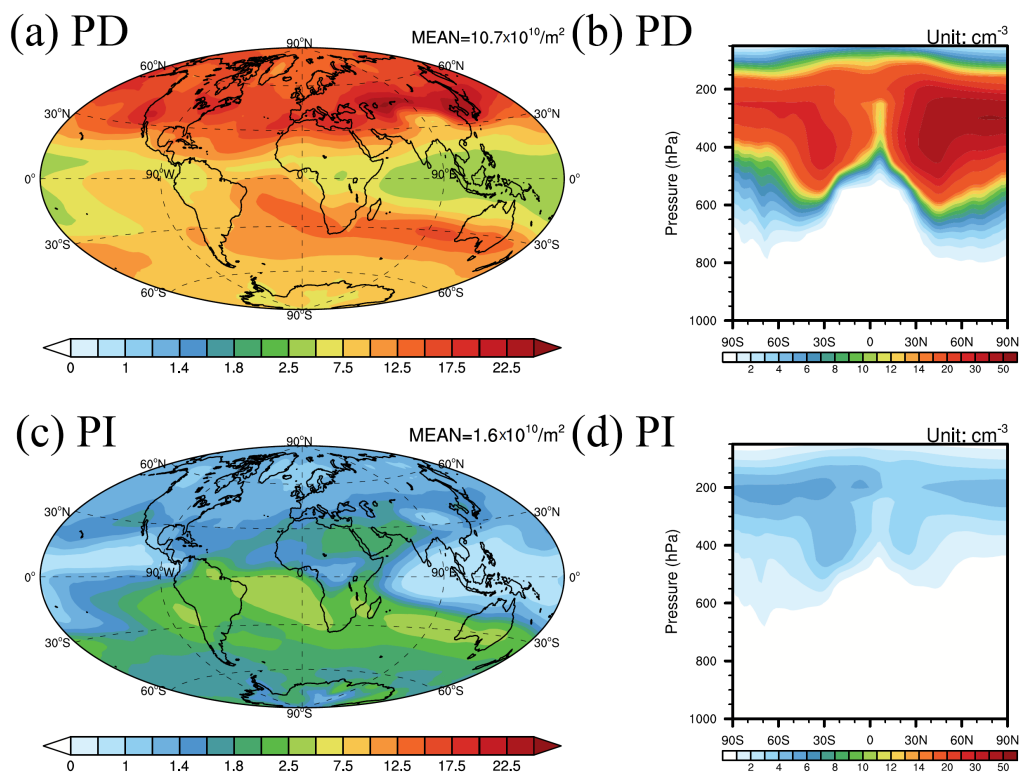
Figure 13. The vertically integrated number of INP (a, c) and zonal average plots of INP (b, d) from SOA in the PD_SOA (a, b) and PI_SOA (c, d) cases.

983

984

985
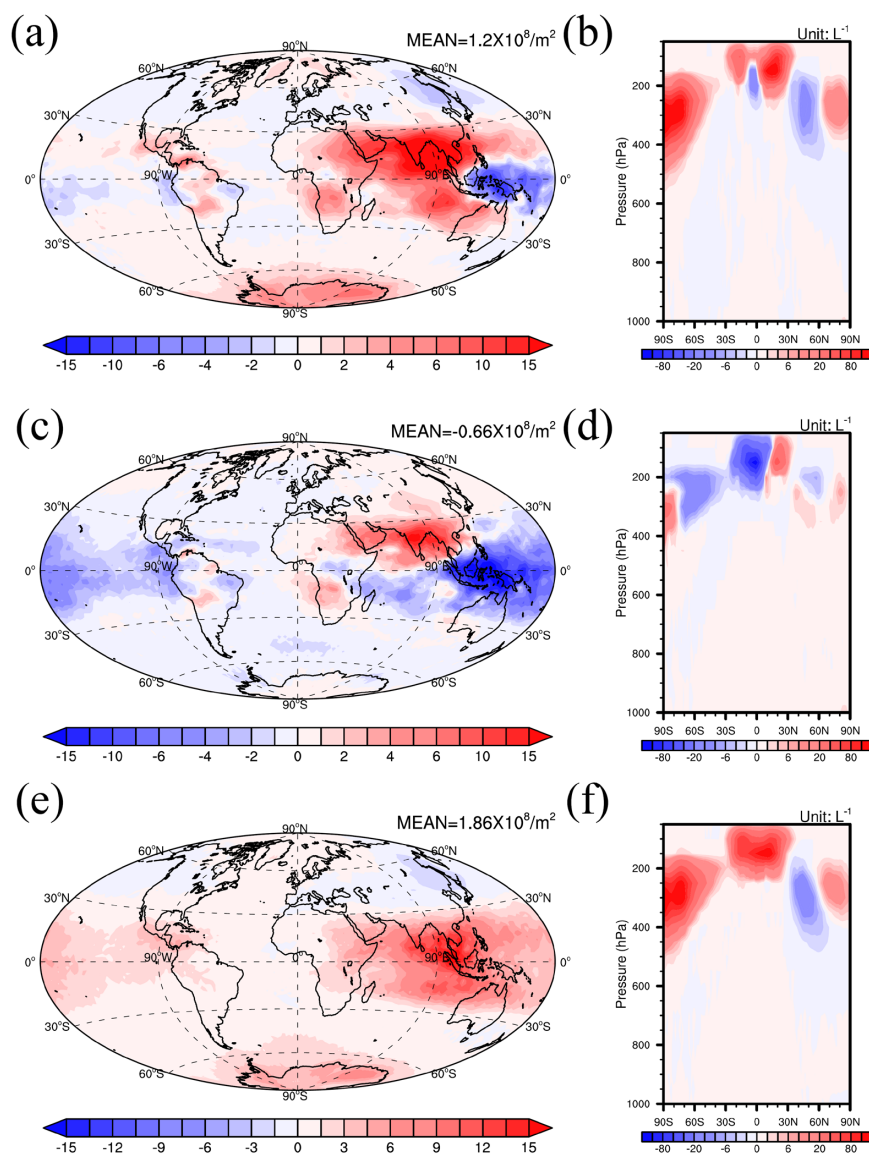
Figure 14. The annual average change in column number concentration (a, c, e)

and zonal average number concentration (b, d, f) of total ice (a, b), ice from

homogeneous nucleation (c, d) and ice from heterogeneous nucleation (e, f) for the

difference between the PD_SOA and PI_SOA cases.
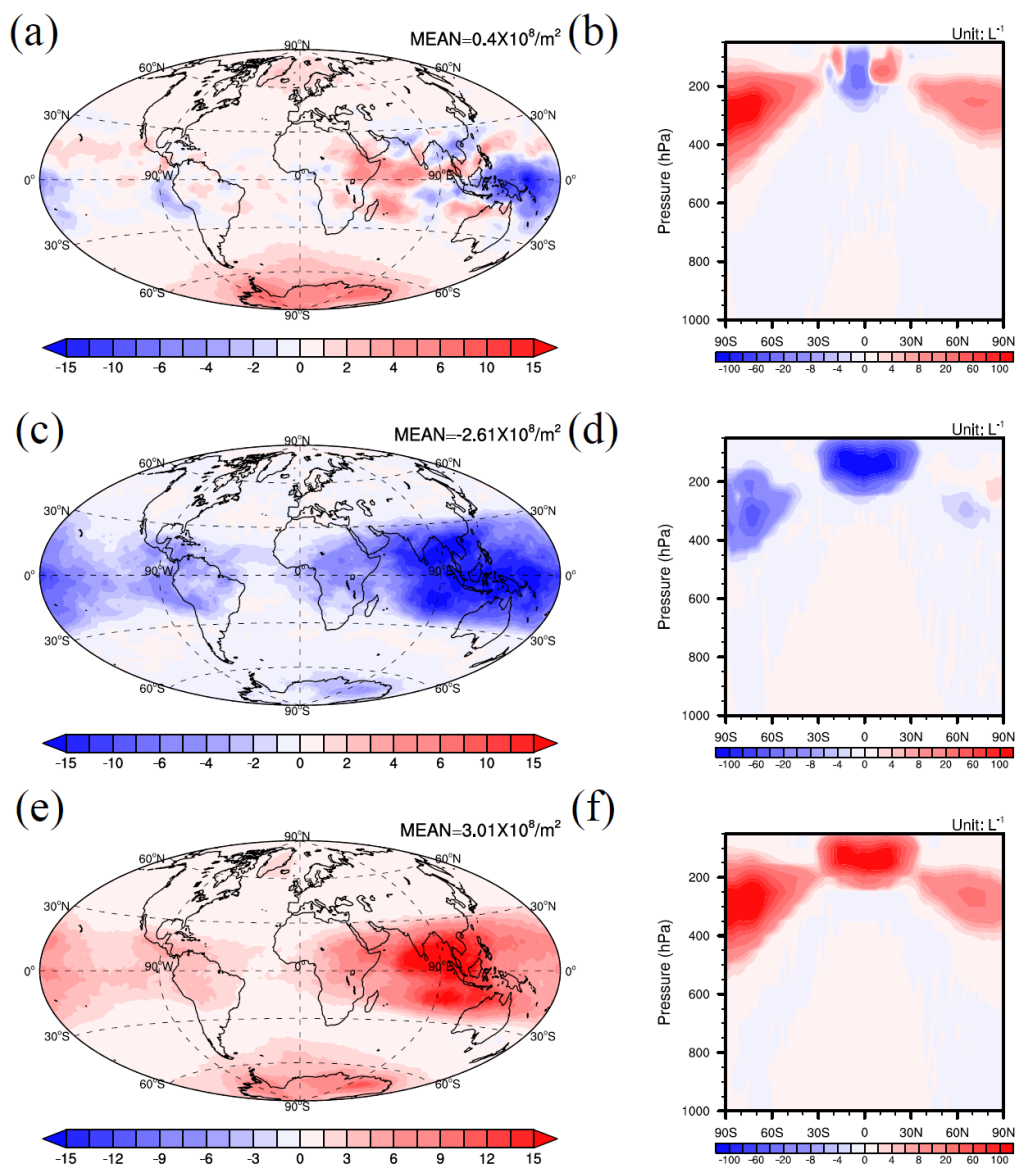
Figure 15. As in Figure 14 but for the difference between the PD_SOA and PD_Base cases.

995
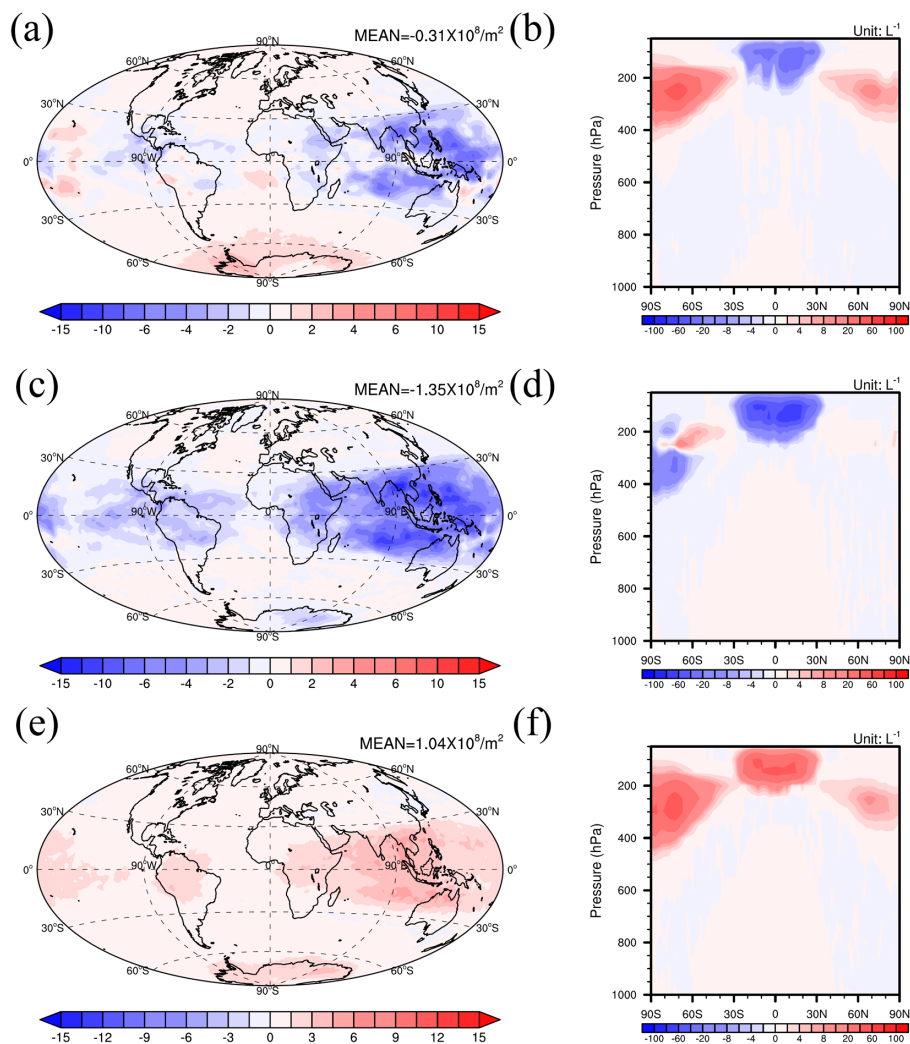
Figure 16. As in Figure 14 but for the difference between the PI_SOA and PI_ALL

cases.

998

999
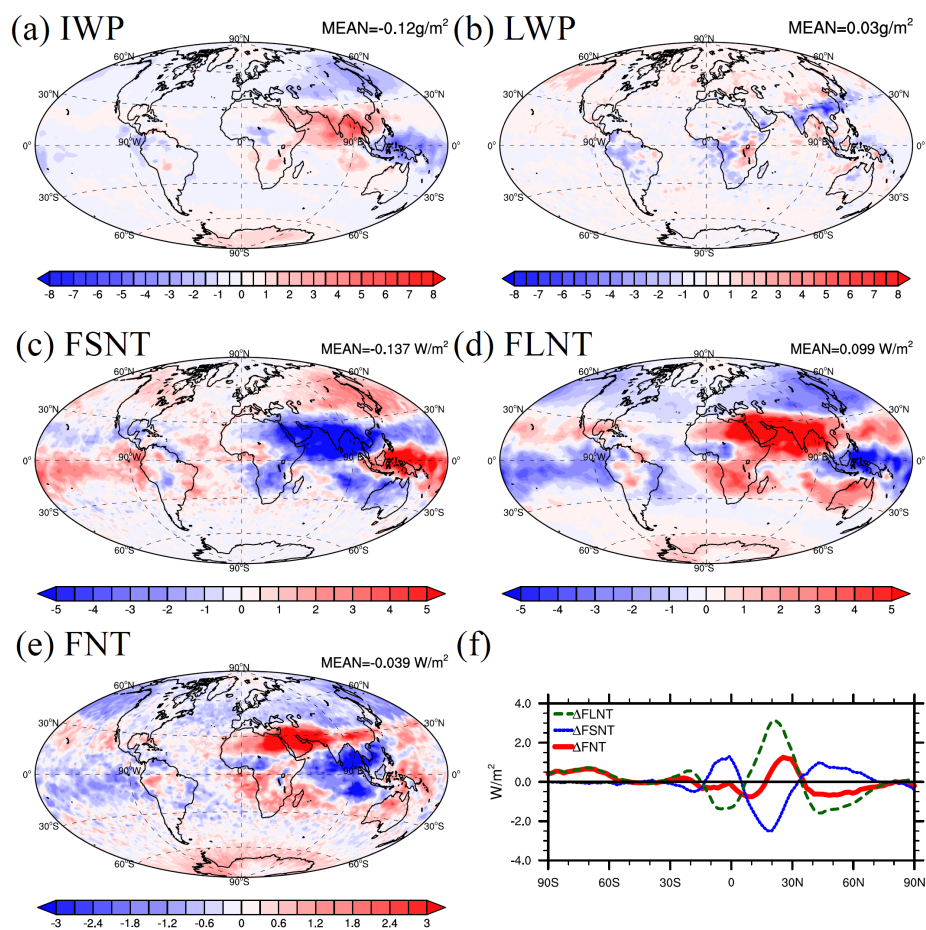
1000

Figure 17. As in Figure 10 but for the difference between the PD_SOA and
PI_SOA cases.

1001

1002

1003

1004
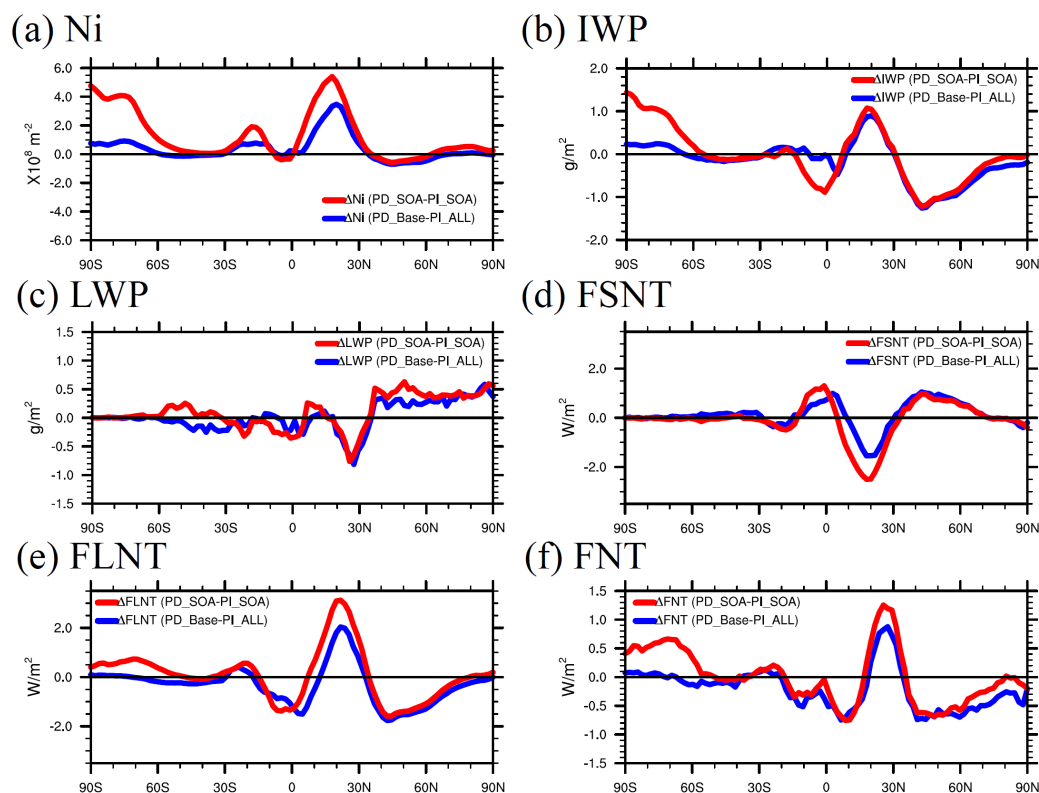
1005

1006   Figure 18. Change in vertically integrated ice number concentration (a), ice water

1007   path (b), liquid water path (c), shortwave effects (d), longwave effects (e) and net

1008   effects (f) for the difference between the PD_SOA and PI_SOA cases (red line) as

1009   well as PD_Base and PI_ALL cases (blue line).

1010

1011

1012

1013

1014